LOCAL DYNAMICS OF SYNOPTIC WAVES IN THE MARTIAN ATMOSPHERE

A Thesis

by

MICHAEL J. KAVULICH JR.

Submitted to the Office of Graduate Studies of
Texas A&M University
in partial fulfillment of the requirements for the degree of

MASTER OF SCIENCE

August 2011

Major Subject: Atmospheric Sciences

Local Dynamics of Synoptic Waves in the Martian Atmosphere

LOCAL DYNAMICS OF SYNOPTIC WAVES IN THE MARTIAN ATMOSPHERE

A Thesis

by

MICHAEL J. KAVULICH JR.

Submitted to the Office of Graduate Studies of
Texas A&M University
in partial fulfillment of the requirements for the degree of

MASTER OF SCIENCE

Approved by:

Chair of Committee,	Istvan Szunyogh
Committee Members,	Mark Lemmon
	Mikyoung Jun
Head of Department,	Kenneth Bowman

August 2011

Major Subject: Atmospheric Sciences

ABSTRACT

Local Dynamics of Synoptic Waves in the Martian Atmosphere. (August 2011)

Michael J. Kavulich Jr., B.S., Worcester Polytechnic Institute

Chair of Advisory Committee: Dr. Istvan Szunyogh

The sources and sinks of energy for transient waves in the Martian atmosphere are investigated, applying diagnostic techniques developed for the analysis of terrestrial baroclinic waves to output from a Mars General Circulation Model. These diagnostic techniques include the vertically averaged eddy kinetic energy and regression analysis.

The results suggest that the primary source of the kinetic energy of the waves is baroclinic energy conversion in localized regions. It is also shown that there exist preferred regions of baroclinic energy conversion. In addition, it is shown that downstream baroclinic development plays an important role in the evolution of the waves and in the baroclinic energy conversion process. This is the first time that evidence for downstream baroclinic development has been found for an atmosphere other than the terrestrial one.

DEDICATION

This thesis is dedicated to thesis dedications everywhere that were crafted with time, love, patience, and sincerity, and now sit unread on dusty shelves and in forgotten archives. I often wonder how many theses are read by people other than the people who wrote them and the members of their committees, and I believe the answer to be "almost none of them." So then, why even take the time to write a dedication? Seems like a bit of time wasted that could be better spent searching for a missing period or stray comma in the 80-page monstrosity I have produced. I guess it's done with the hope that this will serve as a sort of time capsule; that maybe, sometime in the distant (or not-too-distant) future, someone will, in the dark depths of their own research, stumble upon my work, and for some reason stop to read the dedication page. I have the hope, nay the *belief*, that someone will stumble upon my research that consumed my life for a full 2 years, and that the blood, sweat, and tears that I poured into this electronic document will not have been in vain.

So I say to you, researcher of the future, if you are reading this, remember that, although it may seem pointless and trivial now, you are reading my thesis! That means that you, yourself, may one day have someone read your own thesis, and the cycle may continue. Then again, if no one ever reads this, well, then, I haven't made a fool of myself at all, have I?

ACKNOWLEDGEMENTS

I would like to thank my committee chair, Dr. Istvan Szunyogh, for his incalculable patience and invaluable instruction over the past two years. In addition, I thank the other members of my committee, Dr. Mark Lemmon and Dr. Mikyoung Jun, for their willingness to dedicate their time and offer input to my project. Mr. R. John Wilson from the Geophysical Fluid Dynamics Laboratory was indispensible in his guidance on how to use the model and his knowledge of its many intricacies, as was Dr. Gyorgyi Gyarmati, in showing me the ropes on our local computer cluster and for fixing it the (many) times it broke.

A good deal of credit also belongs to the many wonderful teachers and professors I've had over the years: Mrs. Belanger at St. Jude for always believing in me and giving me faith that some teachers truly cared; Mr. Brodeur at St. Jude for showing me (in his own special way) that adults can be just as wrong and thick-headed as children; Mr. Ford at Fairfield Prep for straightening me out when I needed it and for teaching me one of my greatest life lessons: "Physicists are lazy bastards"; and Dr. Iannachione at WPI, for stepping in as my advisor on both my projects and in general being the main reason I was able to graduate on time. These were just the best among many through the years.

A great deal of thanks go out to the awesome group of friends I have stumbled into here at Texas A&M, especially Kelly and Christina, for keeping me sane in this crazy world and not turning me in to the authorities for my various debaucherous misdeeds.

Finally, I'd like to thank my family. I thank my brother and sister for living with me for years without killing me when I would bore them with constant scientific lectures, and for now being among my best friends. And I thank my mom and dad, for always believing in me, encouraging me to be the best I could be, and sacrificing all that they did to help me get to this point.

TABLE OF CONTENTS

LIST OF FIGURES

Page

1. INTRODUCTION

The presence of transient waves in the Martian atmosphere has been theorized since 1877, when Italian astronomer Giovanni Virginio Schiaparelli made observations of "clouds" which obscured different areas of the planet at different times (Sheehan, 1996). We now know that these "clouds" were almost certainly observations of regional dust storms. Over the next close to 100 years, debate raged about the exact nature of the Martian atmosphere. Most of this debate was mere speculation until probes began to return close-up images of the planet. In 1964, Mariner 4 returned several images of the planet that revealed a surface marked by craters rather than seas or plant life, as well as radio-occultation data that, while revealing an atmosphere, showed it to be thin and dry. Mariner 6 and 7 seemed to confirm that the planet was Moon-like and dead. Hope for an interesting, active planet appeared to be lost.

However, in 1971, Mariner 9, which surveyed the entire planet (save the south polar cap) from orbit, observed "yellow clouds associated with a planetary-scale dust storm" (Sheehan, 1996). This was the first indication that Mars had an active atmosphere where powerful storms could exist. Once the planet-wide storm cleared, Mariner 9 observed several regional-scale dust storms, found evidence of water-ice clouds, and even observed front-like cloud formations and cyclonic spirals suggestive of weather systems similar to those observed on Earth (Leovy et al., 1972 and Gierasch et al.,

---

This thesis follows the style of the *Journal of the Atmospheric Sciences*.

1979). Subsequent surface observations by the Viking landers confirmed that transient waves were part of the regular behavior of the Martian atmosphere (Barnes 1981). In the past decade, a wealth of information about the temperature structure of the atmosphere has been returned by the Mars Global Surveyor's Thermal Emission Spectrometer (TES) and the Mars Reconnaissance Orbiter's Mars Climate Sounder (MCS) (Kleinböhl et al., 2009), and it is now established that transient waves are prevalent in the winter seasons of both hemispheres (Hinson and Wilson, 2002; Hinson and Wang, 2010).

In this study, I focus on the transient waves in the Northern Hemisphere. These waves, similar to synoptic waves in the terrestrial atmosphere, develop in response to the meridional temperature gradient in the global atmosphere, which is the result of differential heating of the atmosphere by solar radiation. The process that converts the available potential energy of the atmosphere into the eddy kinetic energy of the waves is called *baroclinic instability*. The basic mechanism of baroclinic instability was first explained successfully by the theoretical work of Eady (1949) and Charney (1947). While these early studies could explain the basic process by which the waves transferred heat and momentum toward the poles, they could not explain many of the observed properties of the waves. In particular, the Eady and Charney models of baroclinic instability correctly predict the wavelengths, but they also predict that the waves should be global structures of wavenumbers 6–8; in reality, the waves develop, propagate, and decay as local features of the atmospheric flow in 5–8-day life cycles. There are also preferred regions, called storm tracks or storm zones, for the development and propagation of the waves. Some waves are deep and are associated with intense surface

cyclones, while some are shallow with a weak signature at the surface. Considering the differences between the terrestrial and Martian atmospheres, it may seem surprising that the life cycles of baroclinic waves in the Martian atmosphere show many similarities with those in the terrestrial atmosphere. Most importantly, there is significant variability in the intensity of the waves and preferred regions of "cyclogenesis" clearly exist (e.g. Read and Lewis, 2004). In this sense, one can talk about "storm tracks" in the Martian atmosphere (Hollingsworth et al., 1996). While the dynamics of the individual waves in the terrestrial storm tracks has been intensely studied, studies of the Martian atmosphere have been limited to studying the time-averaged properties of heat and momentum fluxes associated with the storm tracks (e.g. Barnes et al., 1993 and Hollingsworth et al., 1996). The main goal of the present study is to utilize diagnostic techniques that were developed to analyze the life cycles of baroclinic wave packets in the terrestrial atmosphere, but which have never been applied to the Martian atmosphere before now. These techniques include the local eddy kinetic energy balance equation of Orlanski and Katzfey (1991, henceforth OK91) and the regression analyses of Lim and Wallace (1991) and Chang (1993). I apply these diagnostic techniques to output from the Geophysical Fluid Dynamics Laboratory (GFDL) Mars General Circulation Model (MGCM).

The motivation of this study is twofold. First, the Martian atmosphere offers a unique opportunity to study the dynamics of baroclinic waves in an environment which is very different from the terrestrial atmosphere. I hope that studying the waves in a different environment will enhance our understanding of their dynamics. Second, the

motivation to study transient waves in the Martian atmosphere is more than mere scientific curiosity. Understanding the processes that play a role in the generation, evolution, and sustenance of the transient waves may lead to practical techniques to predict Martian dust storms. These storms are the main hazards to surface operations on Mars. They have been responsible for at least one probe failure—the Russian *Mars 3* lander (Lorenz, 2008)—and can seriously interfere with science missions, e. g. they necessitated the shutdown of both Mars Exploration Rovers during a major dust storm in 2007 (Seibert, et al., 2009). They may also present a significant hazard to more complex and vital operations at the Martian surface, e. g. a manned surface mission (Sharma et al., 2009). Therefore, with the upcoming launch of the Mars Science Laboratory rover, and NASA's plans to perform manned missions to Mars as soon as the 2030s, the abilities to forecast this Martian weather is essential for the success of missions to Mars.

In section 2, I provide background information on the Martian atmosphere and the model. Section 3 describes diagnostic techniques I employ to study the local dynamics of the transient waves. Section 4 describes the results of my experiments. Finally, Section 5 summarizes my conclusions.

2. BACKGROUND

2.1 The Martian atmosphere

The planetary-atmospheric system of Mars can arguably be described as the closest known such system to that of Earth (Leovy, 2001; Haberle 2002). In particular, Mars' length of day (a Martian solar day is referred to as a Sol), and therefore the Coriolis parameter, are similar to those for the Earth. Also similar are the obliquity of Mars's rotational axis, the typical scale height and the Rossby deformation radius in the atmosphere. There are also some important differences between the two planets; in particular, Mars's radius is approximately half of Earth's, the average atmospheric pressure of the mean geoid is less than 1% of average terrestrial sea level values, the main constituent of the Martian atmosphere is carbon dioxide, the atmospheric gas constant is significantly lower than for the Martian atmosphere, Mars's solar constant is less than 50% of Earth's, and this solar constant varies more strongly than Earth's due to Mars's much higher orbital eccentricity. Some physical constants for the Earth and Mars are listed in Table 1.

Table 1: Comparison of properties of Earth vs. Mars. Adapted from Haberle (2002)

	Earth	Mars
Length of solar day	24h 00m 00s	24h 39m 35s
Obliquity	23.5°	25°
Orbital eccentricity	0.0167	0.0934
Scale height	7.6 km	10.2 km
Rossby deformation radius	1150 km	920 km
Mean temperature of lowest scale height	260 K	200 K
Mean surface pressure	1.013×10^5 Pa	~600 Pa
Atmospheric gas constant	287.10 J/(kg·K)	188.92 J/(kg·K)
Average solar constant	1366 W/m^2	590 W/m^2
Typical Brunt–Väisälä frequency	~6×10^-4	~1×10^-2

The Martian atmosphere features only trace amounts of water vapor, and its surface has no permanent liquid water. Its terrain exhibits a striking dichotomy of highlands in the Southern Hemisphere and lowlands in the Northern Hemisphere, punctuated by the large, volcanic Tharsis plateau which straddles the equator (see Figure 1). This dichotomy dictates that waves in the Northern Hemisphere will likely be more intense, with a greater mass of atmosphere due to lower surface terrain (on average 1-3 km lower than the southern hemisphere).

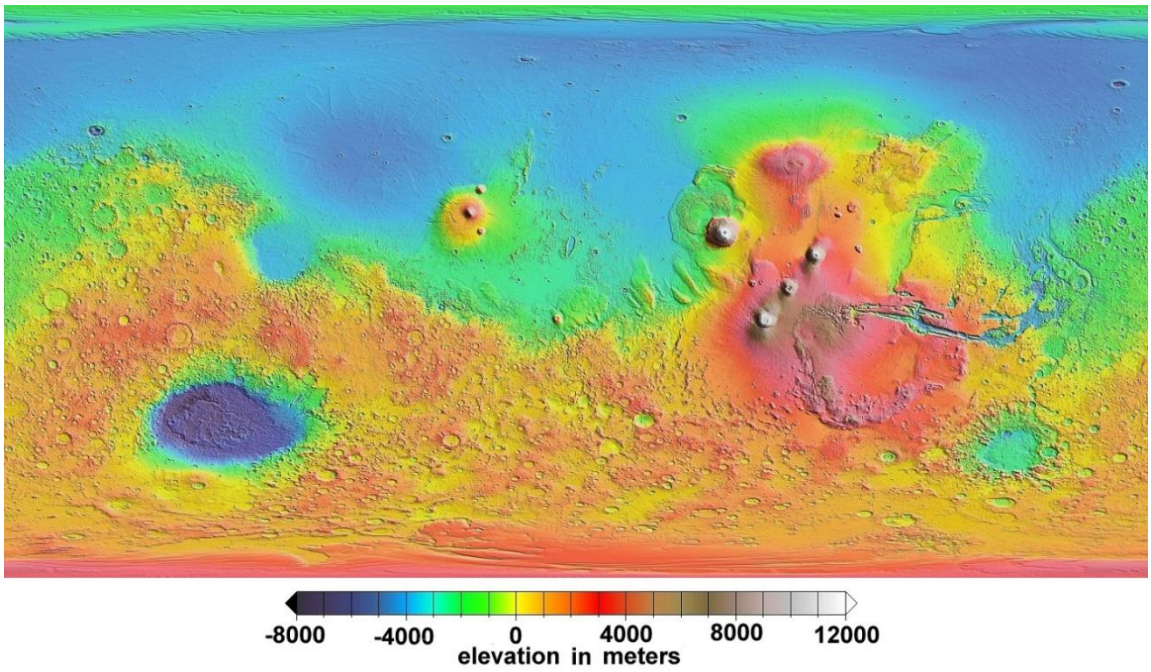

Figure 1: A cylindrical-projection terrain map of the Martian surface. The sides of the image are at the prime meridian, 0°E. The main northern-hemisphere terrain features appear nicely in this color scheme: On the left centered near 50°E is the Arabia Terra highlands, in the center near 150°E is the Elysium Planitia highlands, and at right centered near 260°E is the Tharsis Plateau. Credit: MOLA Science Team, Mars Global Surveyor, NASA (2007).

2.2 The Mars GCM

My implementation of the GFDL MGCM uses a finite volume dynamical core, with an approximately 5° × 6° resolution grid, and 28 vertical levels in a hybrid sigma-pressure coordinate system, which transitions from terrain-following coordinates near the surface to pressure levels near the top, at about 85km height. The model includes radiatively active dust, which is injected into the model using a simple dust-devil parameterization. Typical visible-light optical depth values in the model range from 0.1-0.3, with the highest values near the equator at lower elevations, which is roughly in

agreement with observations, keeping in mind that this model cannot explicitly resolve dust storms (Smith, 2009).

My diagnostic calculations are based on data obtained by a cold-start nature run of the model at perihelion, which is at solar longitude L_s=251°, where L_s=0° is the northern hemisphere spring equinox, L_s=90° is the northern hemisphere summer solstice, etc. In the nature run, a realistic climate develops, in response to the proper physical constants and realistic time-dependent forcing terms, after less than 100 Sols. In this study, I only analyze data from the Northern Hemisphere winter period. For some of the diagnostic calculations, I use data from a 17000 Sol-long (approximately 25 Martian years) period. My initial investigation, however, is for a ~100-sol period centered on the Northern Hemisphere Winter Solstice.

2.3 Isolating the signal of the transient waves

Due to the lower thermal inertia of a waterless planet, the diurnal cycle in the state variables is much more pronounced in the Martian atmosphere than on Earth. The diurnal cycle is particularly strong near the surface. Therefore, to isolate the signal of the

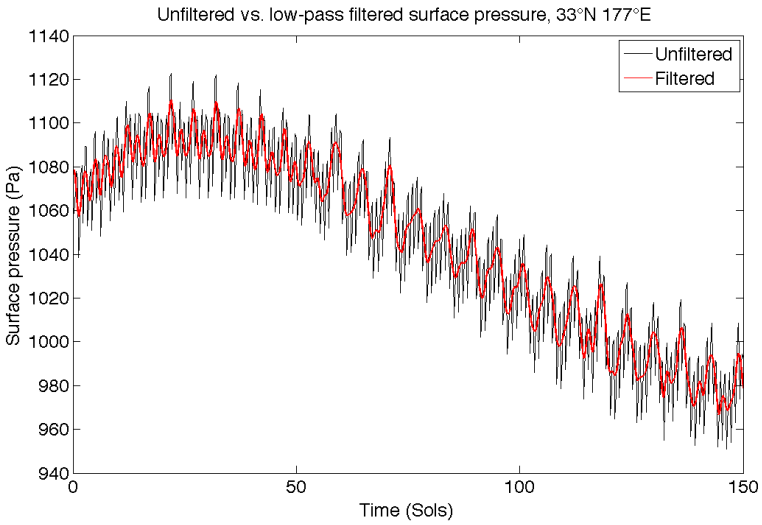

Figure 2: Digitally filtered diurnal cycle. This plot is a comparison of a time series of surface pressure from the model output to the same data with a low-pass digital filter applied to remove the diurnal cycle (see text for filter description). The time series is 150 Sols surrounding the Northern Hemisphere winter solstice in the model's first full winter for the point 33°N 177°E, which was chosen arbitrarily as a good example of strong diurnal variation. The signal from transient waves with periods of 2-4 sols becomes much clearer after the filtering.

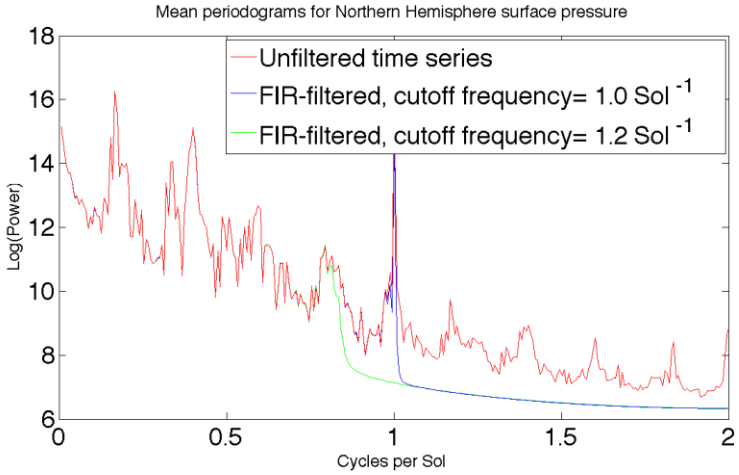

Figure 3: Periodogram showing effect of digital filter. This figure shows the periodograms for the surface pressure in the Northern Hemisphere for the same period as Figure 2. Waves with frequencies lower than ~0.8 per sol are unattenuated in all cases, thus only one line appears. Note that the x-axis is log(Power).

transient synoptic waves, I apply a low-pass filter to all variables, removing all signals of frequency 1 Sol^{-1} or higher (see Figure 2). The filter I use is a 50th-order Hamming-window type filter, with a cutoff frequency of 1/1.2 Sol^{-1}. This cutoff frequency of slightly lower than 1.0 Sol^{-1} is chosen because the attenuation of the diurnal cycle with a 1.0 Sol^{-1} cutoff frequency is insufficient. The cutoff frequency 1/1.2 Sol^{-1} was found by numerical experimentation; it eliminates the diurnal cycle efficiently while leaving the frequencies of interest intact (Figure 3).

In addition to the strong diurnal cycle, Mars features a strong seasonal variation in all the state variables (Figure 4). This is due to many factors, most notably the deposition and sublimation of up to 30% of the atmospheric mass in the polar ice caps over the course of a year (James et al., 1992). Therefore, the seasonal trend must also be removed from the time series. Previous studies have used 2nd- (Barnes 1980) and 3rd-order (Murphy and Nelli, 2002) polynomials to model the seasonal trend in the data. This motivated us to test 2^{nd}- and 4^{th}-order polynomials to capture the seasonal trend in the time series (Figure 5). While the polynomial approach captured the seasonal trend reasonably well for short (~100 Sol) timespans, fitting the polynomials for longer periods became cumbersome. Thus I settled on using a running mean with a period of 30 Sols (15 Sols before and after each time step of interest).

2.4 The background flow

In my diagnostic calculations, the 30-day running mean defines the background flow. Next, I illustrate the properties of this background flow. Typical vertical profiles of

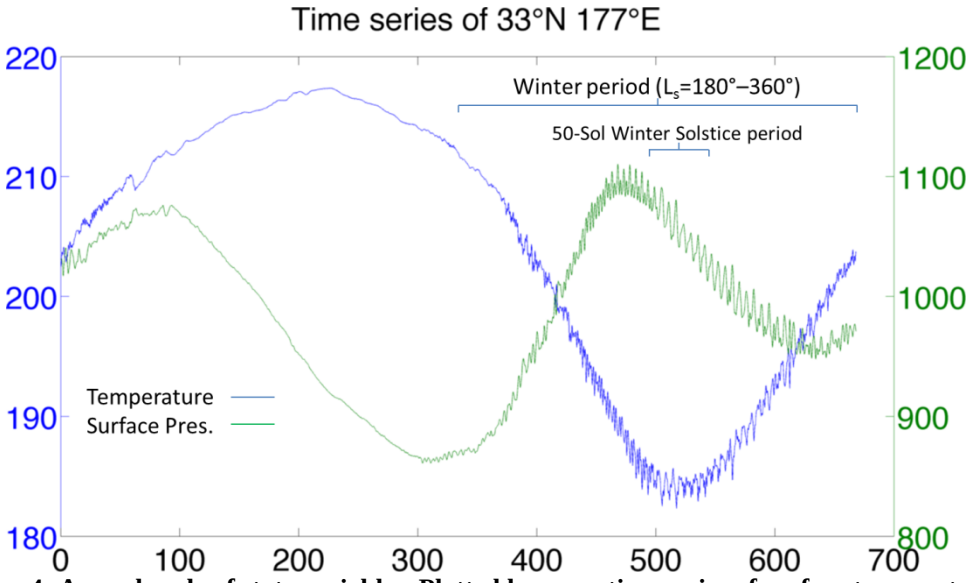

Figure 4: Annual cycle of state variables. Plotted here are time series of surface temperature in Kelvin (blue) and surface pressure in Pascals (green) for the first full Martian year of our model run (spring equinox to spring equinox). Different time periods referred to in this paper are highlighted.

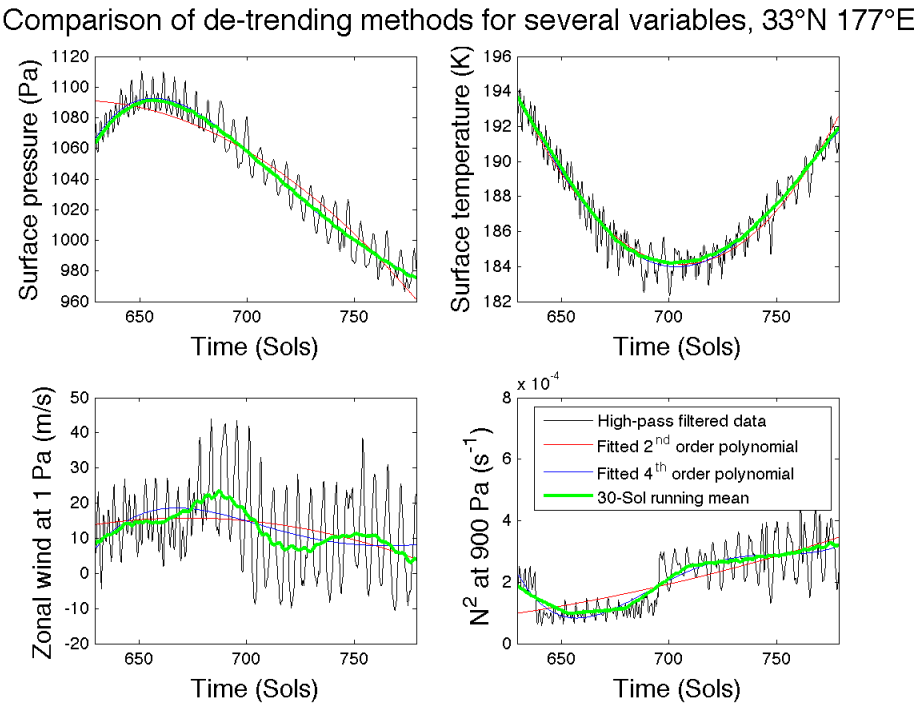

Figure 5: A comparison of different methods to remove the seasonal trend from different variables. The x-axis is the number of Sols since the start of the nature run (winter solstice is Sol 704). All time series are shown for the point 33°N 177°E.

the temperature, the zonal wind, and the Brunt-Väisälä frequency are shown in Figure 6. The atmosphere is essentially isothermal for the lowest scale height, indicative of a very convectively stable background state. This conclusion is also confirmed by the Brunt-Väisälä frequency, which is positive throughout the atmospheric profile. It is important to note that in the lower levels of the atmosphere the diurnal temperature cycle is quite intense, so this diurnally-filtered "background" temperature profile may not be representative of the typical Martian atmosphere. Indeed, it has been shown that, especially in the boundary layer, the temperature profile can vary from an extremely stable inversion to an unstable superadiabatic layer over the course of a single Sol (Smith et al., 2004). However, it is safe to say that the background state is generally very stable, as this has been the conclusion of previous modeling and observation studies (Read and Lewis, 2004).

The zonal wind speed increases with height, up to about 200 Pa in the mid-latitudes and to around 1 Pa in the higher latitudes, which indicates that the jet has a northerly tilt. The background temperature (Figure 7) is generally dominated by the expected north-south temperature gradient one would expect for the middle of winter, where the polar night extends as far south as 65°N. As with the terrestrial atmosphere (e. g. Holton, 2004), the polar front is tilted northward with height, however, without the stratospheric inversion of the terrestrial atmosphere, the polar front in the Martian atmosphere extends to much higher altitudes. Due to an orography where the peaks are much higher than on Earth, surface heating is very important to the low- and mid-level temperature distribution, and leads to zonally asymmetric pattern. In addition, the high

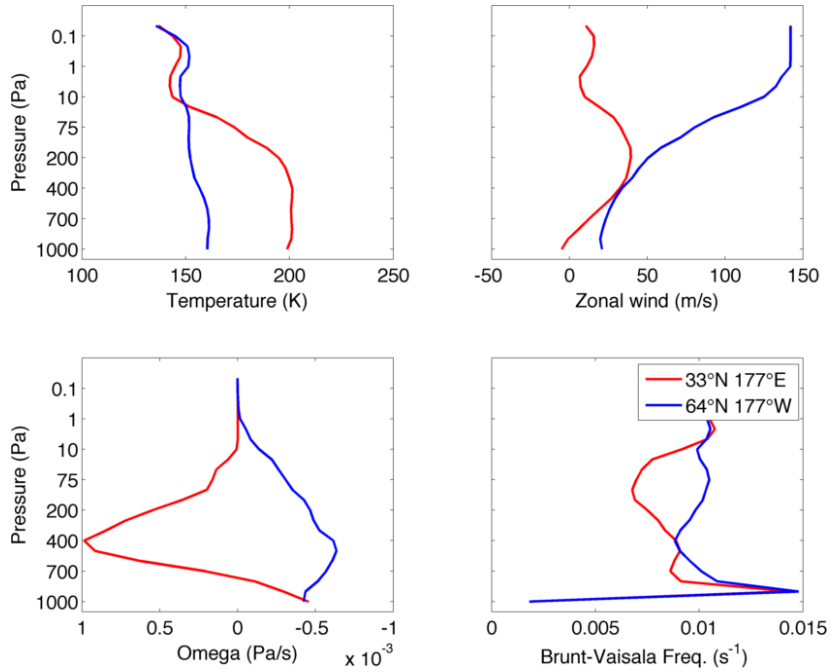

Figure 6: Time mean vertical profiles of state variables. A selection of time-mean vertical profiles of variables in the mid-latitudes (red) and for a representative point in the higher latitudes (blue). The time period is the same as Figure 5.

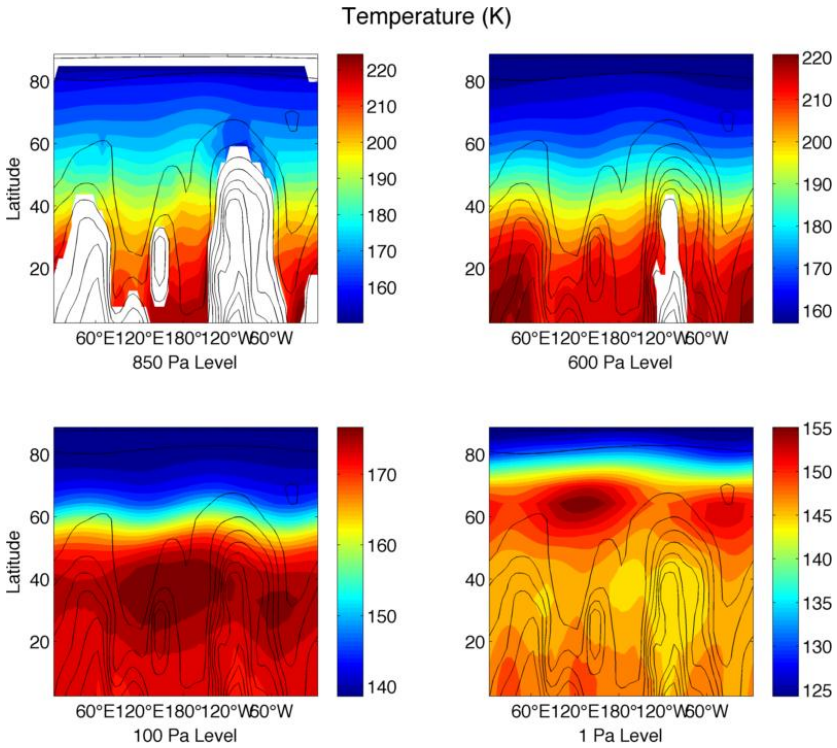

Figure 7: Winter-long mean temperature at several pressure levels.

terrain in the Northern Hemisphere follows a roughly zonal wavenumber 2 pattern, which excites a wavenumber 2 standing wave pattern in the background flow, as can be seen well into the upper levels of the atmosphere.

The two components of the wind vector in the background state are shown in Figures 8 and 9. The jet has a similar structure to the mean structure of the terrestrial polar jet; it is tilted polewards, and the vertical wind shear is in thermal wind balance with the strong meridional temperature gradient along the front. Similar to the temperature fields, the low-to-mid-level horizontal velocity is heavily influenced by the terrain variations, and higher levels display the same standing wave pattern as seen in the temperature background, with crests over the Tharsis highlands near 120°W and Arabia Terra near 50°E.

The background omega, or vertical velocity for pressure coordinates in Pa/s, is shown in Figure 10. In the terrestrial atmosphere for large scale analyses such as ours, the background state can be assumed to have zero vertical velocity. This is not true of the Martian atmosphere, which exhibits large areas of persistent and strong subsidence (on the same order of magnitude as eddy fluctuations) in the low- to mid-levels downstream of the large terrain features Arabia Terra (50°E), Elysium Mons (150°E) and the Tharsis plateau (120°W). There is also a clear wavenumber 2 pattern associated with the orography.

To measure the baroclinic instability of the background flow, I use the Eady index, σ, introduced by Hoskins and Valdes (1990). The Eady index is the growth rate of the most unstable baroclinic mode, that is, $\sigma = 0.31 \frac{f}{N} \frac{\partial U}{\partial z}$, where f is the Coriolis

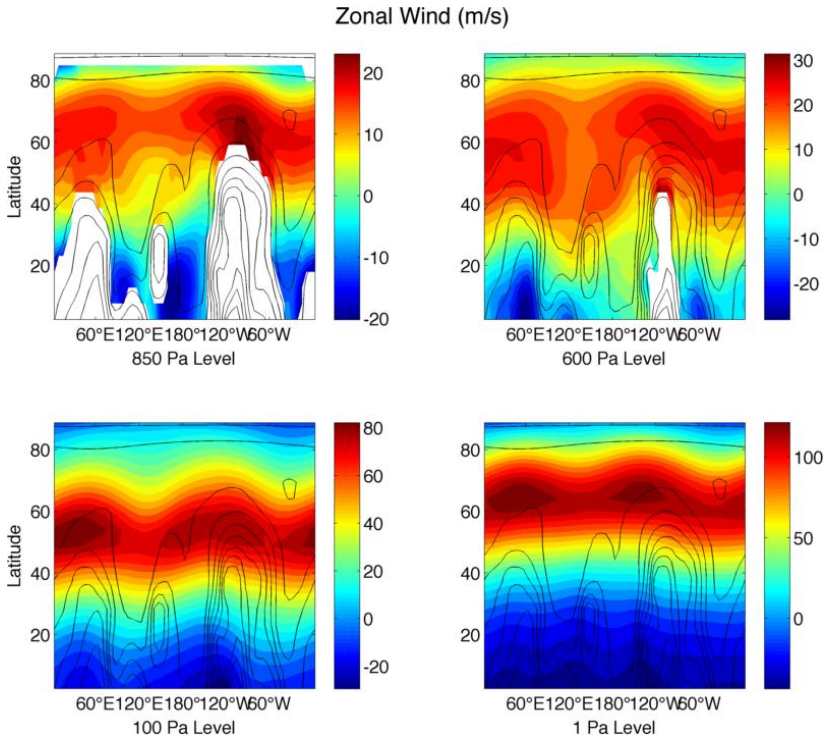

Figure 8: Same as Figure 7, but for the zonal wind velocity.

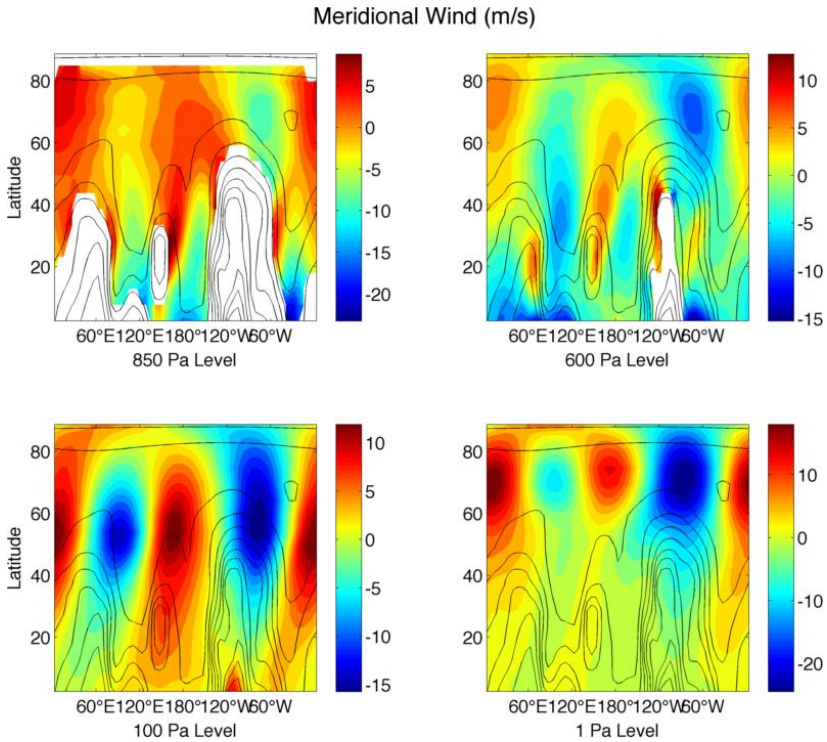

Figure 9: Same as Figure 7, but for the zonal wind velocity.

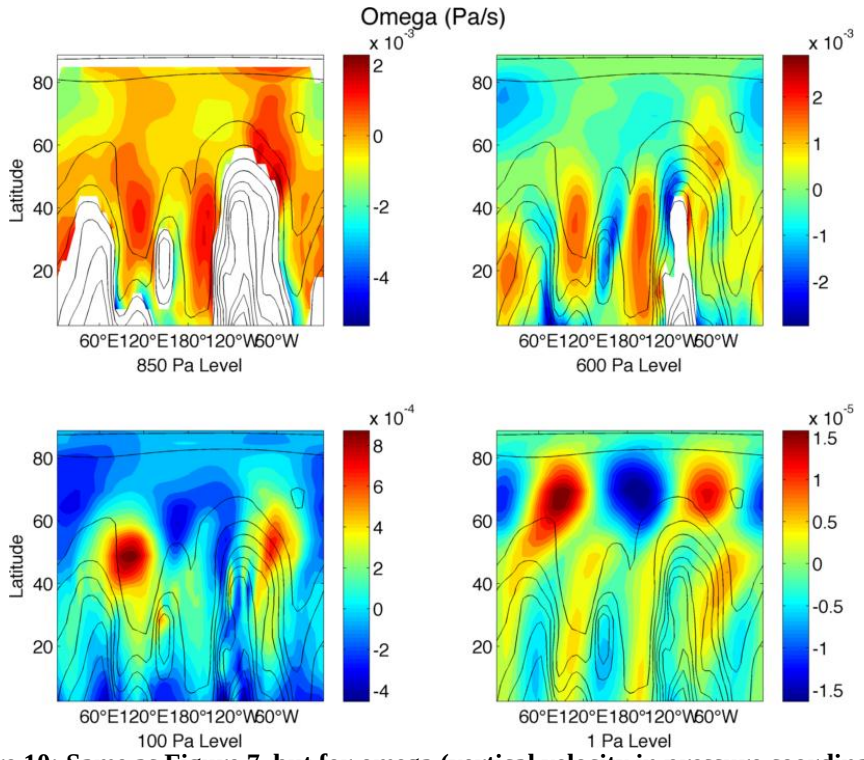

Figure 10: Same as Figure 7, but for omega (vertical velocity in pressure coordinates).

parameter, N is the mean Brunt–Väisälä frequency, and $\frac{\partial U}{\partial z}$ is the vertical shear of the background flow. The larger the Eady index, the stronger the baroclinic instability in the flow. A map of the Eady index for the 975 Pa pressure level is shown in Figure 11. The two regions of largest instabilities are around 60°E and 100°W, north of the large terrain features Arabia Terra and the Tharsis plateau, respectively. Based on experience for the terrestrial atmosphere (e. g. James 1994), I expect that the main regions of kinetic energy generation by baroclinic instability will be located downstream of the maxima of the Eady index.

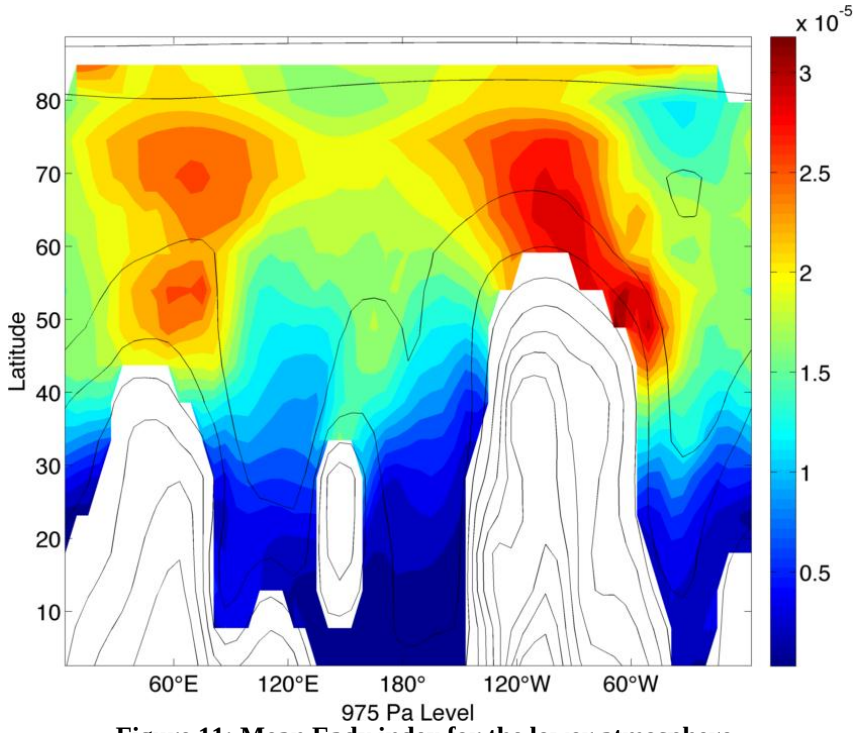

Figure 11: Mean Eady index for the lower atmosphere.

2.5 Time-averaged properties of the transient waves

Transient waves occur in the Northern Hemisphere for roughly the period from equinox to equinox (Ls=180°–360°). This is the period that I designated as "winter" in Figure 4. The propagation of the transient waves is illustrated by Figure 12, which shows a Hovmöller diagram for the 50 Sols centered on the Winter Solstice. The variable used to visualize the waves here is the meridional eddy velocity, defined by the deviation of the meridional component of the wind from its 30-Sol running mean, at the approximate center of the jet level (1 Pa). Figure 12 shows a wave number 1–2 wave packet traveling around the planet with a quire regular period of 5-6 Sols. This behavior is different from that shown by the transient baroclinic waves in the terrestrial atmosphere, which can rarely complete a full circuit around the planet. While the Martian waves rarely form,

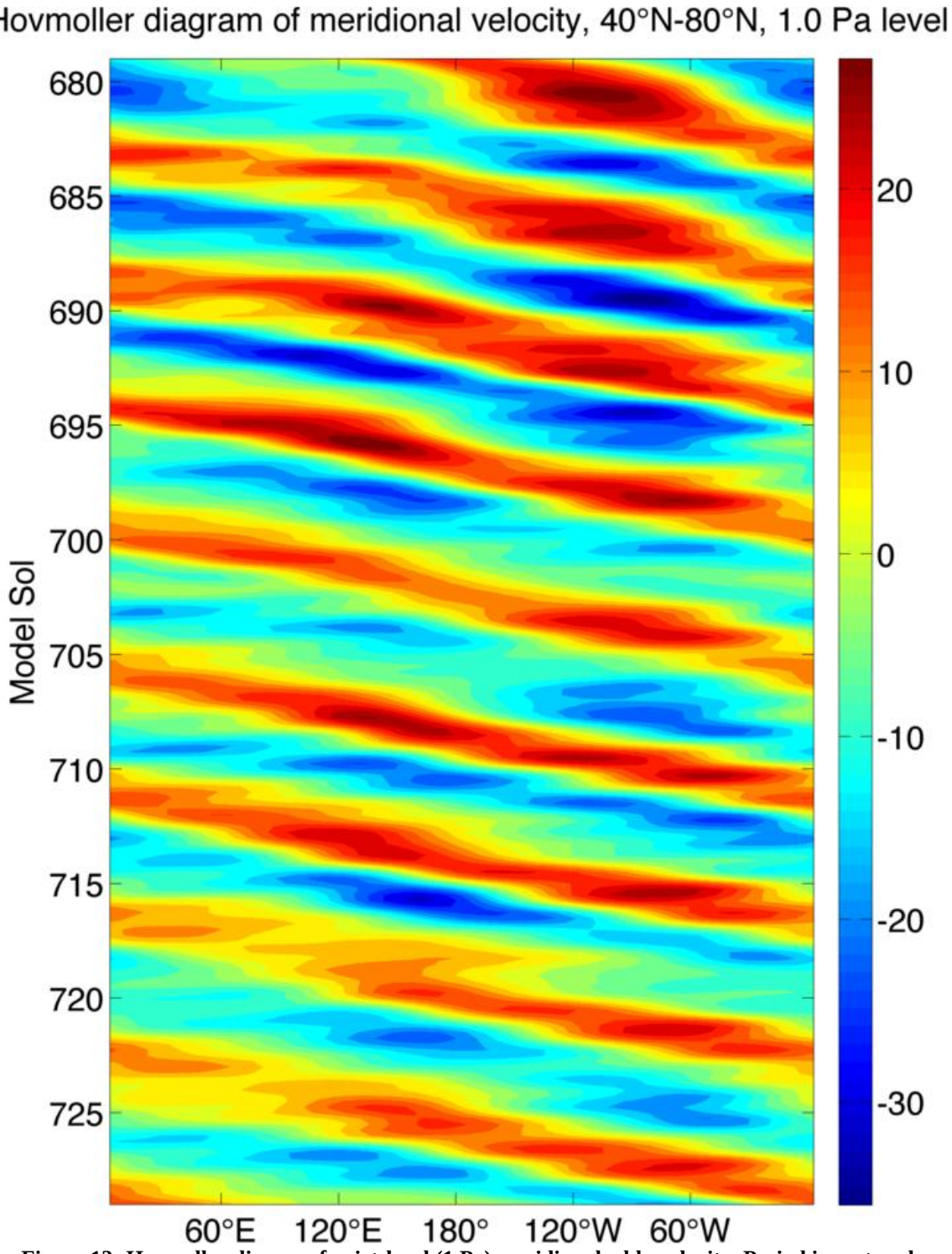

Figure 12: Hovmoller diagram for jet-level (1 Pa) meridional eddy velocity. Period is centered around Winter Solstice, which is on model Sol 704.

grow, and decay in a single planetary transit, there are typical regions of amplification and weakening: the wave amplitude typically amplifies around 100°E and 60°–80°W and weakens elsewhere. These maxima are even more clearly visible in the winter-long mean of the eddy kinetic energy at jet level (Figure 13). The locations of the two maxima in the average eddy kinetic energy are just downstream of the maxima of the Eady index. This seems to confirm that the maxima in the eddy kinetic energy are due to baroclinic instability. A more careful investigation, however, reveals that while the primary maximum centered around 150°E is certainly due to baroclinic energy conversion, the secondary maximum around 80°W is due to a different process. I come to this conclusion by investigating the period meridional temperature flux, $\overline{v'T'}$, and vertical temperature flux, $\overline{\omega'T'}$. Baroclinic energy conversion takes place where the

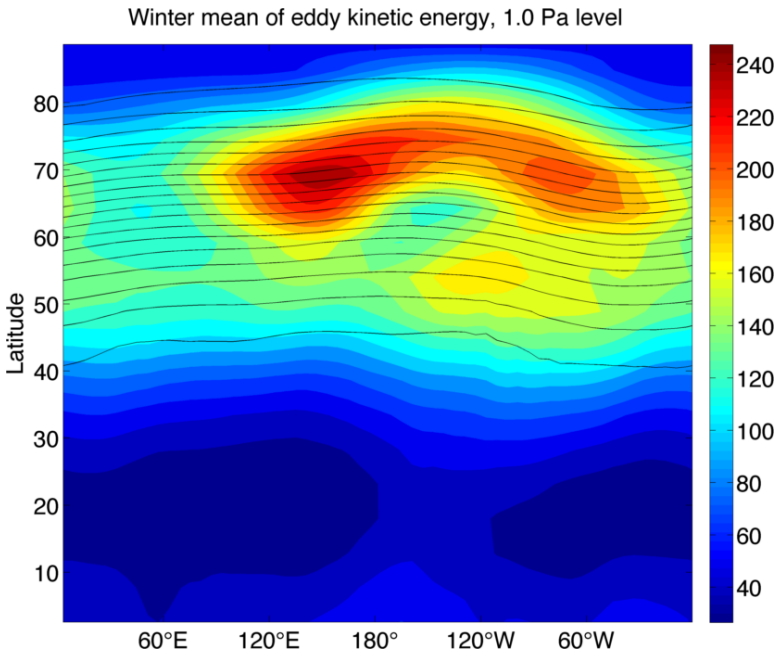

Figure 13: Plot of winter-long mean of eddy kinetic energy for the jet level (1 Pa). Period centered on winter solstice. Contours are in units of m^2/s^2.

former is positive and the latter is negative. Figures 14 and 15 show that the aforementioned condition is met between about 50°E and 160°W (There is also a secondary region of baroclinic energy conversion centered on 25°W); but no baroclinic energy conversion takes place between 210°W and 60°W. In fact, Figure 15, which shows a local maximum of equatorward heat flux in the layer between 200 Pa and 10 Pa, indicates that a very different process plays the dominant role in the local dynamics in that region. Since an equatorward heat flux cannot occur spontaneously, and the region is north of Tharsis which features the highest terrain on the planet, orographic forcing clearly plays an important role.

2.6 Illustration of a wave event

I now turn my attention to the spatio-temporal evolution of the transient waves. Figure 16 shows an example of an eastward propagating synoptic wave. The right column shows the deviation from the running mean surface pressure, while the left column shows the deviation from the running mean meridional velocity at the 1.0 Pa level, which is the approximate center of the jet level in the Northern Hemisphere winter (Read and Lewis, 2004). From the top down, the panels show the perturbations at Sols 688–692.5, at half-Sol (12-hour) intervals. In the meridional wind, a clear, positively tilted trough is apparent for the entire period, with its axis around 30°W in the first panel. The surface signature of this trough, while close to vertically stacked in the first panel, is quite elongated. In most of the model's waves, the surface low is elongated when passing north of elevated terrain; this is likely due to the fact that higher elevations

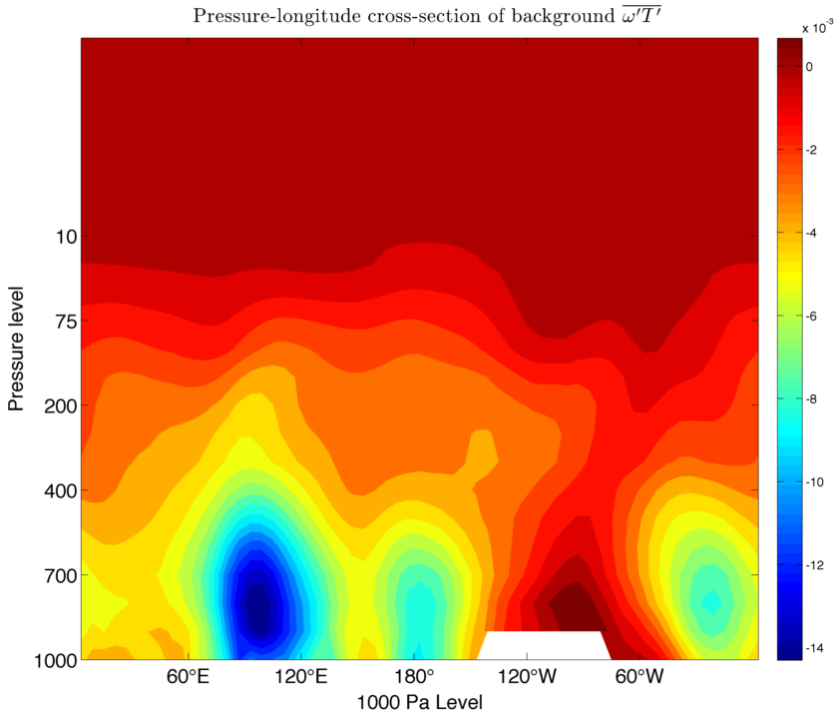

Figure 14: Pressure-longitude plot of 50-Sol mean of w'T', 60°N. This latitude circle was chosen due to being roughly the center of the main storm zone.

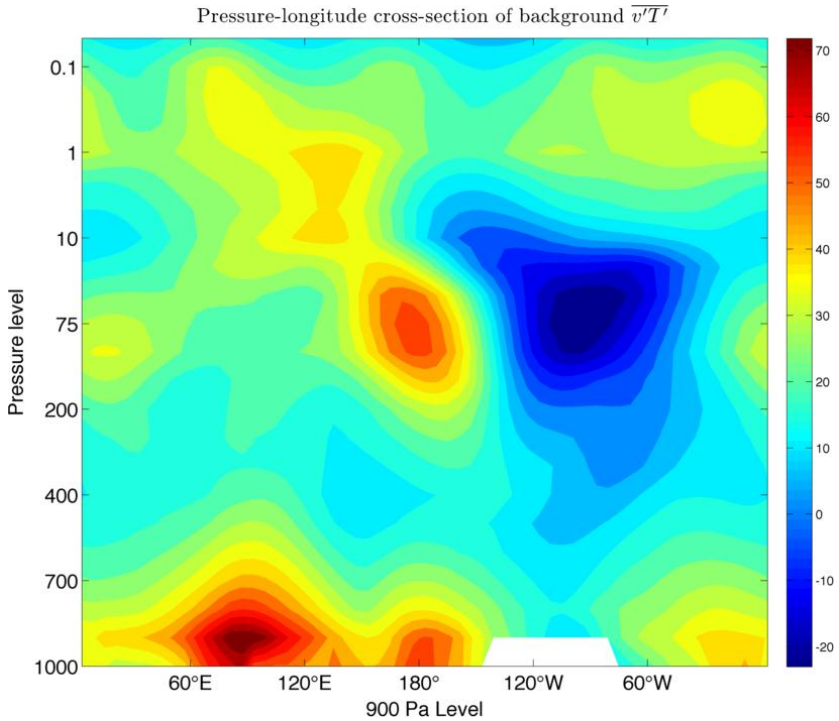

Figure 15: Same as Figure 14, except for v'T', 60°N.

have lower ambient surface pressure, and thus the same deviations will be of a lesser magnitude. Over the first 24 Martian hours, both the jet-level and surface waves propagate eastward. A secondary, weaker upper-level trough also appears around 100°E in panel 3. On Sol 687.5 (panel 4), the upper-level trough has begun to intensify, while the surface pattern has reached its peak intensity, with both the low- and high-pressure centers having reached their maximum intensities. In addition, the secondary upper-level trough has become better defined, and by Sol 688 the entire Northern Hemisphere is essentially in a wavenumber 2 pattern. By Sol 688.5 (panel 6), the main upper-level trough axis has continued to intensify and travelled eastward, now centered near 170°E, while the weaker trough appears to be weakening, now centered near 50°E. The surface center has become indistinct, with two possible minima, one near 75°N 20°E and another, north-south elongated center near 100°E. Twelve hours later on Sol 689, the main trough axis has reached its maximum intensity for the period, and has moved very little, centered near 160°W. Meanwhile, the secondary surface low is becoming better defined and moving east-northeast. By Sol 689.5 (Panel 8), the secondary trough has become ill-defined, located near 60°E but very low in amplitude. Yet while the jet level is transitioning to a wavenumber 1 pattern, the surface pressure continues to show two distinct minima, the first of which has deepened rapidly and is quite distinct near 60°N 170°E, while the other appears to be the remains of the old center from Sol 1 and is centered near 75°N 40°E, but is elongated and weak. On Sol 690 (Panel 9), the upper-level pattern has continued to de-amplify, with the main trough still having not travelled very far to the east (now centered near 170°W), and the surface low has reached its peak

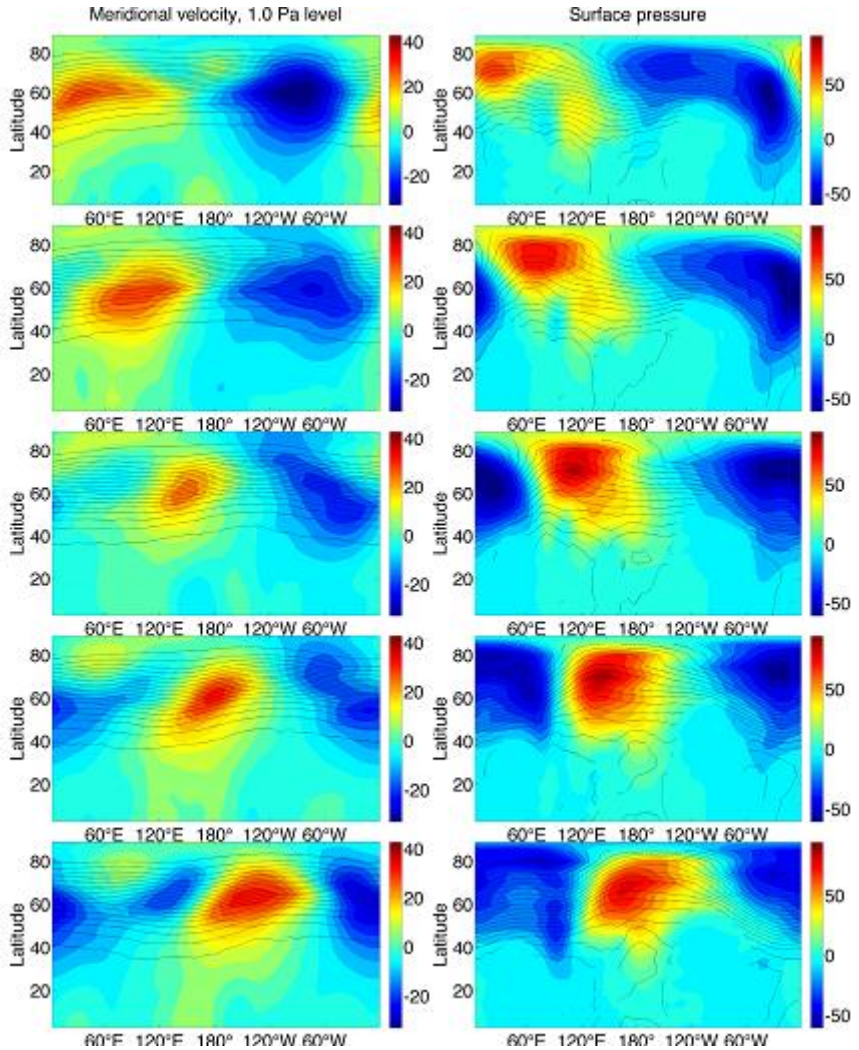

Figure 16: An example of an eastward-travelling synoptic wave in the Northern Hemisphere winter. Specifically, at model Sols 686-690.5 at half-Sol (12-hour) intervals. The series of images on the left show the deviation from the running- mean meridional velocity (color contours, m/s) at the 1 Pa level, or roughly the center of the jet stream. The right column shows the deviation from the running-mean surface pressure (in Pa). Geopotential height contours (black isolines) are shown in black on both plots, on the left for 1 Pa (contour interval approximately 700 m, southernmost contour 55.8 km above the mean geoid) and on the right for 800 Pa (contour interval approximately 125 m, southernmost contour approximately 750 m below the mean geoid).

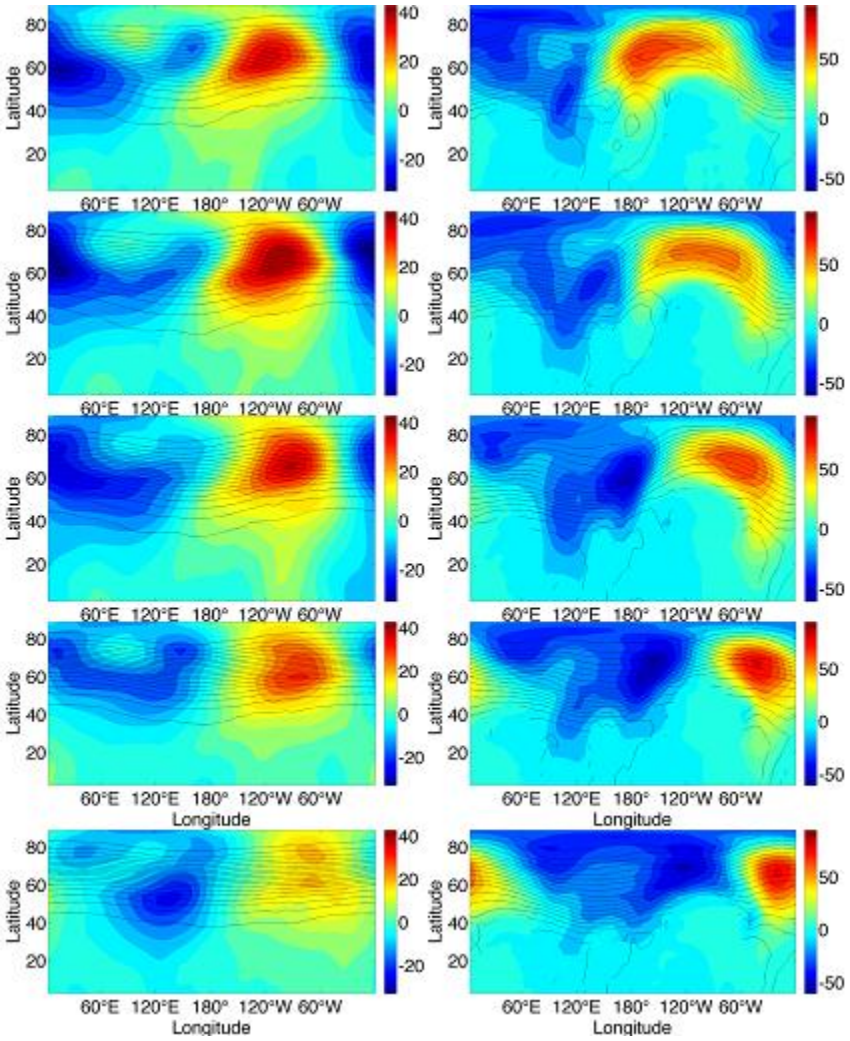

Figure 16: Continued.

intensity near 70°N 160°W. Finally, on Sol 690.5 (bottom panel), the upper-level pattern has continued to decay into a weak wavenumber 1 pattern, while the surface pressure contains a strong minimum which is moving quickly east near 70°N 120°W behind a strong maximum near 65°N 20°W, along with a weak trough centered near 90°E which is the remnant of the old low pressure center from the beginning.

The patterns at the surface and aloft evolve similarly, with the features all moving at approximately the same phase speed. Additionally, both the upper and lower levels appear to be transitioning between a wavenumber 1 and wavenumber 2 pattern. A look at longer-term data (not shown) reveals that this wave is indeed where the general pattern of waves at jet level switches from wavenumber 2 to wavenumber 1. This type of intransivity is well-documented in the Martian atmosphere (Read and Lewis, 2004; page 168).

Figure 17 shows the same wave as Figure 16, but in a vertical cross-section at 60°N. The right-hand column is now the eddy geopotential height. The meridional velocity features a strong negatively-tilted upper-level wave which travels eastward through the period changing very little, with a much weaker trough at the surface which travels eastward at around the same speed. The height field also features a strong upper-level pattern, with a ribbon of negatively tilted positive height extending westward and accelerating, before dissipating while a neutrally tilted height maximum descends from the upper-level maximum.

Similar to Figure 17, Figure 18 shows a cross-section at 60°N, but this time showing the meridional heat flux ($v'T'$) in the left column and the vertical heat flux

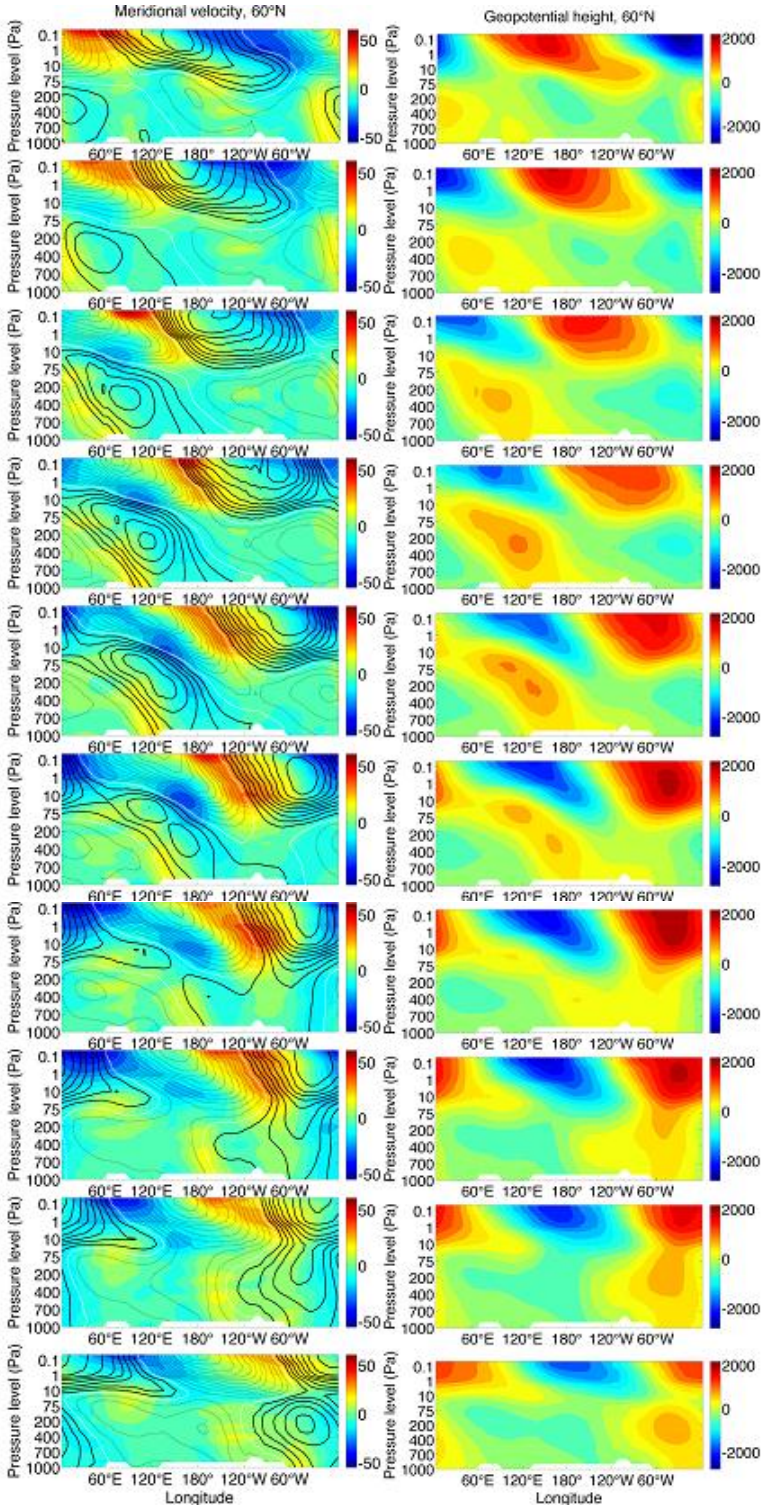

Figure 17: Same time period as Figure 16, but a pressure-longitude plot. The left column is still deviation from the running-mean meridional velocity, but now the right column is the deviation from the running-mean pressure heights, as a three-dimensional analog of the surface pressure.

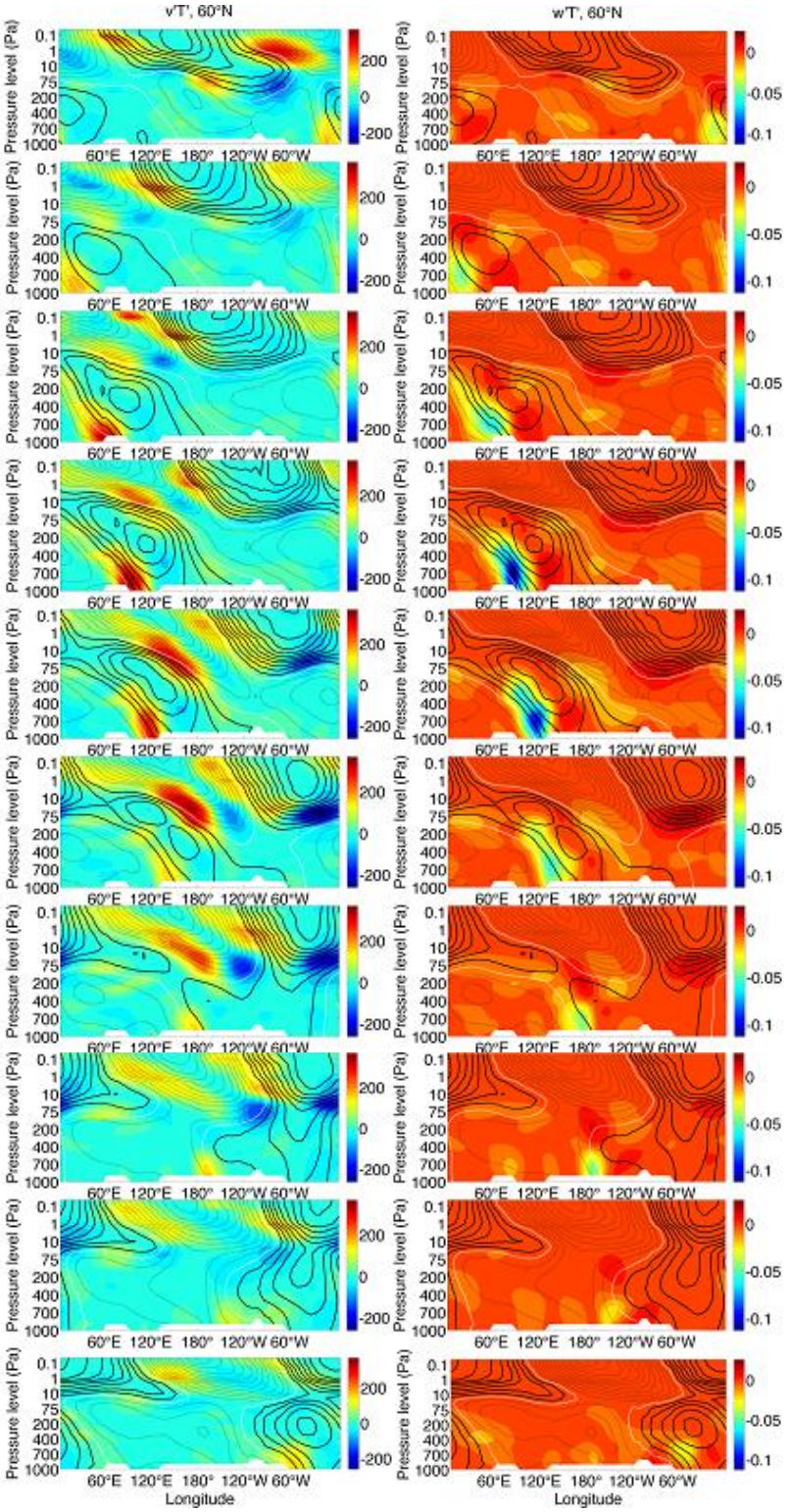

Figure 18: Same time period as Figure 17. The left column is meridional heat flux, and the right column is the vertical heat flux, both indicating areas of baroclinic energy conversion.

($\omega'T'$) in the right column. The main feature of interest is a bulls-eye of baroclinic energy conversion (positive $v'T'$ and negative $\omega'T'$) in the lower levels near 80°E. This feature travels westward ahead of the surface trough, and while it decreases in intensity it remains distinct through all three Sols (and indeed, looking at additional timesteps, the growth area never disappears completely, but does weaken considerably further from the main zone near 100°E from Figure 14. This zone will be examined in more detail later).

Next, I use the Hilbert-transform-based method introduced in Zimin et al. (2003) to study the wave packet shown in Figure 16. This method extracts the amplitude (envelope) of the wave packet in a prescribed wavenumber range. Figure 19 is obtained by extracting the envelope for the wavenumber range 1–3.

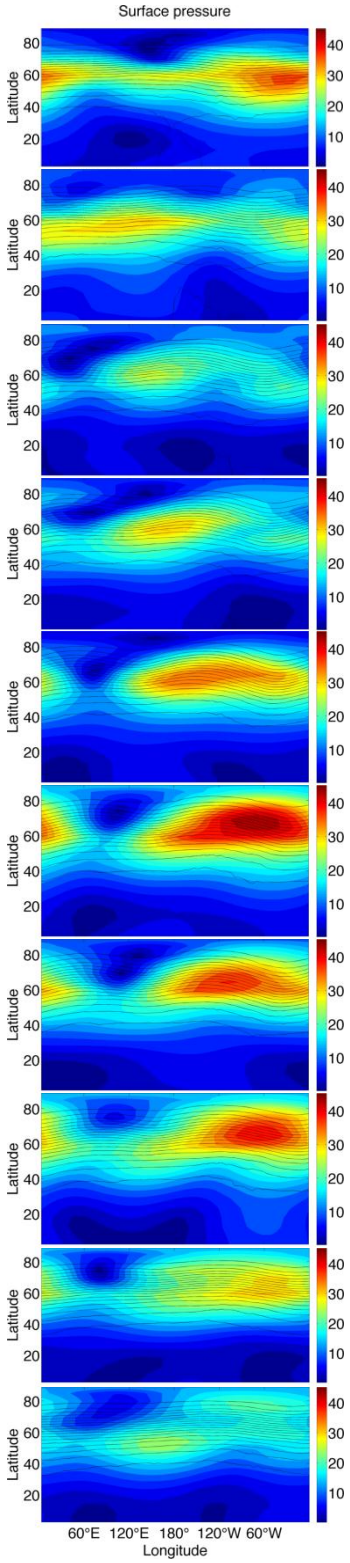

Figure 19: Wave packet analysis for the same time period as Figure 11. This is a horizontal plot of the Hilbert-transform-based wave packet analysis taken at 60°N.

3. METHODS

3.1 Local eddy kinetic energy budget

The eddy kinetic energy balance equation of OK91 identifies the different processes that generate and destroy eddy kinetic energy in a hydrostatic atmosphere. To derive the equations, all state variables are decomposed into a basic flow and a perturbation component. For instance, an arbitrary state variable Ψ is written as $\Psi = \Psi_{\mathbf{M}} + \psi$, where $\Psi_{\mathbf{M}}$ is the basic flow component and ψ is the perturbation. In my case, this basic flow is defined by the 30-Sol running mean. The kinetic energy can then be partitioned as

$$K = \frac{1}{2}\mathbf{V_m}\cdot\mathbf{V_m} + \mathbf{V_m}\cdot\mathbf{v} + \frac{1}{2}\mathbf{v}\cdot\mathbf{v} = K_m + K_1 + K_e \tag{1}$$

where the first term on the right side is the kinetic energy of the basic flow, the second term is a first-order correlation term, and the third is the *eddy kinetic energy* (EKE). This last term represents the kinetic energy of the transient features in the atmospheric flow.The vertically averaged eddy kinetic energy equation of OK91 is

$$\frac{\partial}{\partial t}\langle K_e\rangle = -\overbrace{\langle\nabla\cdot\mathbf{V}K_e\rangle}^{1} - \overbrace{\langle\nabla\cdot\mathbf{v_a}\phi\rangle}^{2} - \overbrace{\langle\omega\alpha\rangle}^{3} - \overbrace{\left\langle\mathbf{v}\cdot(\mathbf{v_3}\cdot\nabla_3)\mathbf{V_m} - \mathbf{v}\cdot\overline{(\mathbf{v_3}\cdot\nabla_3)\mathbf{v}}\right\rangle}^{4} - \overbrace{[\omega K_e]_s + [\omega K_e]_t}^{5} - \overbrace{[\omega\phi]_s + [\omega\phi]_t}^{6} + \overbrace{\langle\text{Residue}\rangle}^{7} \tag{2}$$

where chevrons, $\langle\cdot\rangle$, indicate a vertical average in pressure coordinates, and brackets $[\cdot]$ indicate the surface integral across the surface (subscript *s*) or top (subscript *t*) pressure surface. A detailed derivation of Eq. 2 can be found in Oczkowski (2003). Each term in Eq. (2) represents a different form of energy conversion: Term 1 is the advection of eddy

kinetic energy by the basic flow, and is sometimes called the *energy transport* term; Term 2 is the *ageostrophic geopotential flux convergence*, which represents the conversion between the potential energy and the eddy kinetic energy of the wave; Term 3, which is positive when warm air is rising or cold air is sinking, is the component of the *baroclinic energy conversion*, which converts the available potential energy of the wave to eddy kinetic energy; Term 4 represents the *barotropic energy conversion*, which is the transfer of kinetic energy between the mean flow and the wave; Term 5 represents the vertical advection of eddy kinetic energy; and Term 6 is related to the vertical flux at the bottom and top of the model atmosphere. The final "Residue" term encompasses all other unaccounted sources and sinks of eddy kinetic energy, which includes the forcing of the mean background flow, interpolation errors, frictional effects, other subgrid processes and the potential contribution of the processes related to the filtered diurnal cycle. Terms 5 and 6 have been shown to be negligible for the terrestrial atmosphere, and I found that the same was true for the Mars GCM. The residue term, which I determine by calculating the difference between $\frac{\partial}{\partial t}\langle K_e \rangle$ and the sum of the other terms on the right hand side, is non-negligible. At most locations, the residual term is negative, indicating that this term is typically dominated by frictional effects.

The one term that requires some additional explanation is the *ageostrophic geopotential flux convergence*. Traditionally this term attracted little attention, as it does not appear in the spatially integrated form of Eq. 2 for the globe. OK91 and subsequent studies (e. g. Chang and Orlanski, 1993; Orlanski and Sheldon, 1995) have shown, however, that this term often plays the role of the trigger in the development of

baroclinic waves in the terrestrial atmosphere. This process is usually referred to as *downstream baroclinic development*, or simply downstream development. The role of this term has never been investigated before for the Martian atmosphere.

3.2 Vertical structure of Martian transient waves

Because the OK91 analysis considers vertically-averaged terms, I will need to use additional diagnostics to detect vertically propagating influences associated with the waves. For this purpose, I adopt the approach of Lim and Wallace (1991) and Chang (1993), who used regression analysis to detect connections between the jet-level wind and the different state variables at different atmospheric levels. The regression is constructed by starting with a reference time series $x_t(i), i = 1,2, \dots, N$ which is created by taking a time series of a selected variable at a given point and then dividing each data in the time series by the square root of the variance of the time series. The regression coefficient is then given by

$$b_j = \frac{1}{N}\sum_{i=1}^{N} y_j(i)x_t(i) \tag{3}$$

where b_j is the j-th regression coefficient, N is the number of observations in the time series and $y_j(i)$ is the non-normalized time series of another variable against which the regression is performed. The regression coefficients can also be shifted in time and/or performed for spatial fields of variables, so a more general form of (3) would be

$$b(t,x,y,z) = \frac{1}{N}\sum_{i=1}^{N} y(i+t,x,y,z)x_t(i) \tag{4}$$

In Equation 4, $b(t, x, y, z)$ is a regression coefficient, which depends on both space and time. The larger $b(t, x, y, z)$ at a given time and location, the larger the influence of the variable represented by x_t on the variable represented by y at the given time and location. The regression analysis enables us to analyze the strength of the typical relationships between variables at different times and locations in the Martian transient waves. Of special interest is the problem of whether the waves start to develop by processes near the surface or their development is triggered by downstream development as often happens in the terrestrial atmosphere.

4. RESULTS

4.1 Local energetics

I first analyze the local energetics in my simulation run for a 50-Sol period around the winter solstice in model year 2 (the first full winter). I will refer to this as the "Winter Solstice period" in the interest of brevity. The time- and vertically averaged eddy kinetic energy for this period confirms the existence of "storm tracks" (Figure 20, top panel). The pattern I find is in good agreement with that reported by Hollingsworth et al. (1996): the area of highest eddy kinetic energy is northwest of the Tharsis plateau, at latitude 60°N and between longitudes 180°E–220°E. A secondary maximum is located around latitude 55°N, between longitudes 110°E–150°E. This pattern suggests that transient waves gain energy as they move east-southeast over the lowlands of Utopia Planitia (roughly 80°E–130°E), and they lose some of their energy as they turn east to the north of the Elysium volcanic highlands (around 150°E), then turn east-northeast and

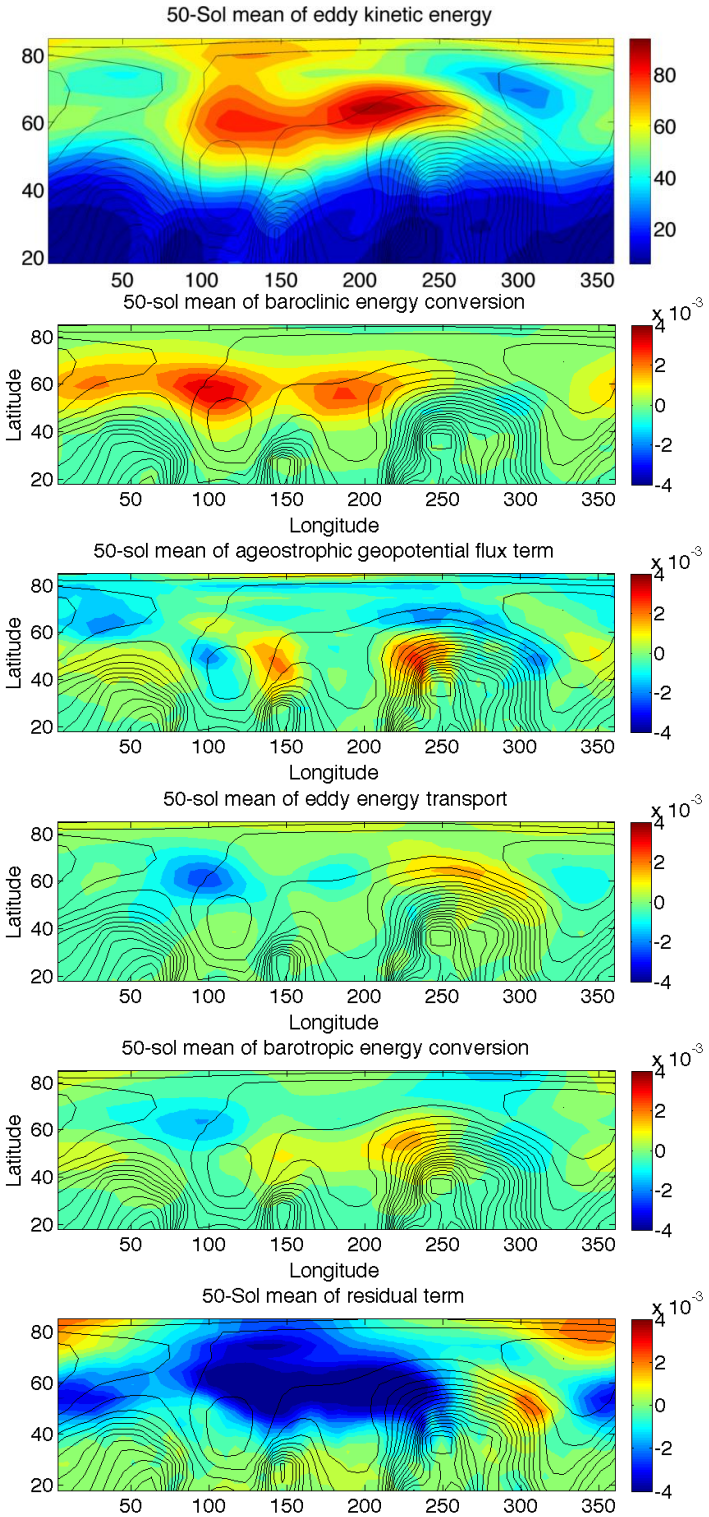

Figure 20: Average eddy kinetic energy (top panel) over a 50-Sol period. This period is centered on the winter solstice, showing enhanced areas of EKE or "storm zones". Black contour lines are of surface elevation, with EKE contours are in units of J/kg (m2/s2).

grow to maximum strength northwest of the Tharsis plateau. The waves then decay rapidly as they travel north of Tharsis.

These are not subtle maxima; there is a pronounced decrease in eddy kinetic energy to the east and west of the storm tracks, with distinct *minima* to the northeast (near 65°N 300°E) and northwest (70°N 50°E). In addition, there is a sharp cutoff to the south, with EKE values decreasing sharply south of 50°N. Another weak maximum occurs near 75°N 130°E, with enhanced eddy kinetic energy also occurring near the poles. These maxima are due to the quick-moving waves which occur at high altitudes along the polar front during this period.

With sharp zonal asymmetries in the time-averaged eddy kinetic energy, I would expect that there must be geographically persistent sources and sinks of energy. Taking the time-means of the terms on the right hand side of Eq. (2), it is apparent that this is indeed the case. The lower five panels of Figure 20 show the 50-Sol means of the different terms. The dominant source of eddy kinetic energy is baroclinic energy conversion. The baroclinic energy conversion term has multiple maxima; the most intense one, located near 60°N 100°E, is co-located with the area of the strongest gradient in the eddy kinetic energy.

The energy transport term has a pronounced minimum upstream of the storm track, as well as a maximum downstream of the storm track. The barotropic energy conversion term is the smallest of the four terms, and appears to be generally positive to the north and west of the high terrain features. There is one bulls-eye of barotropic

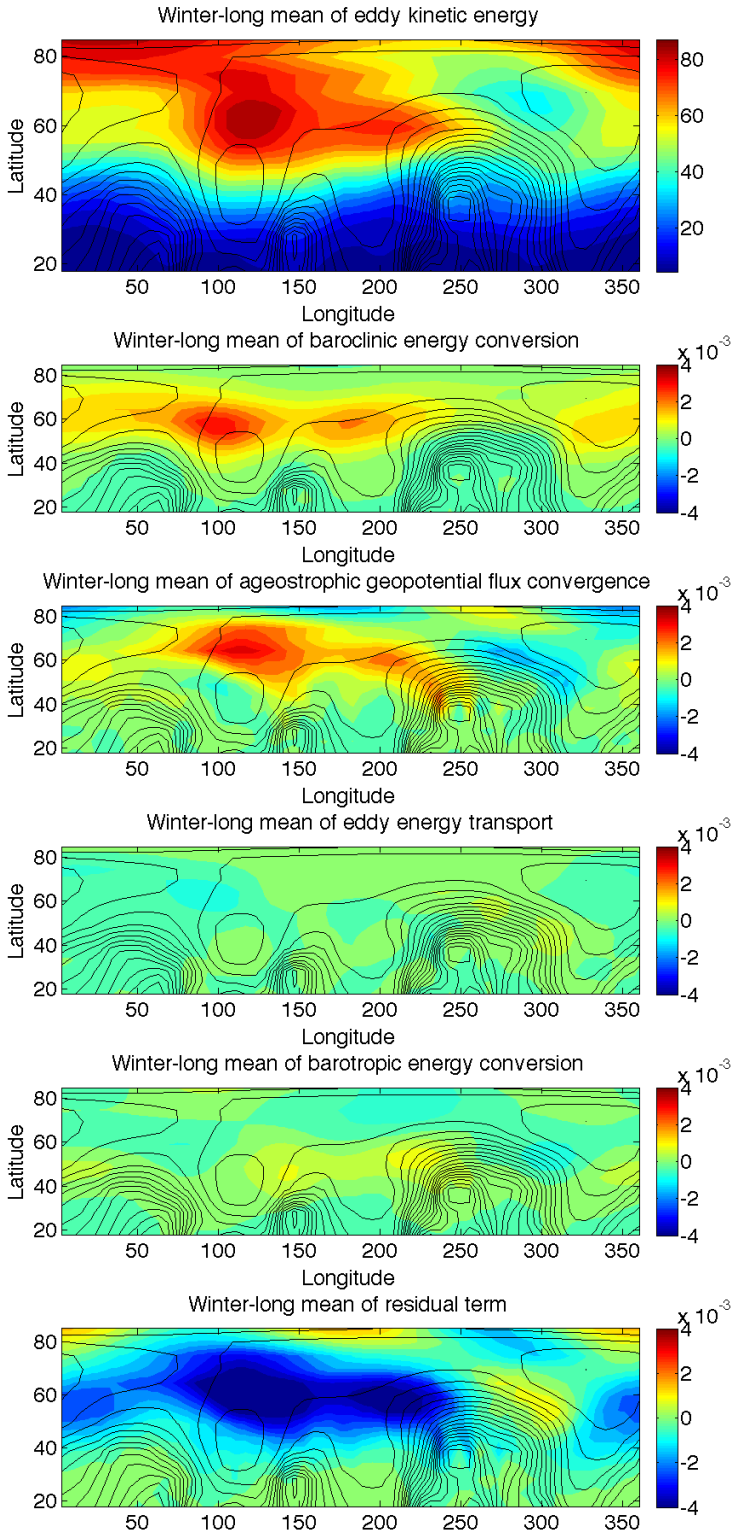

Figure 21: Same as Figure 20, but averaged over the entire winter period. This winter period is defined as 180°<Ls<360°.

decay, apparently co-located with the area of most intense baroclinic growth, but of much smaller magnitude.

Another significant term is the ageostrophic geopotential flux convergence: the two most intense maxima are both north/northwest of high terrain. Apart from these maxima, there are very few striking features in this plot. There is a broad area of negative contribution from this term north and east of the Tharsis plateau, suggesting that ageostrophic flux convergence is at least partially responsible for the decay of the waves during the investigated period.

The final significant term is the residual term. In previous studies for the terrestrial atmosphere, this term was often found to be significant (e.g. Oczkowski 2003). Indeed, the same is true for my calculation. In particular, the residual term is by far the largest negative contribution to the eddy kinetic energy budget. I will further address this point later on.

Figure 21 shows the same diagnostics as Figure 20, but the time averaging is done for the entire Northern Hemisphere winter period (the first full model winter, defined as L_s=180°–360°), as this is the period of highest transient wave activity in the Northern Hemisphere. In the longer average, the general storm track area is about the same as for the 50-Sol mean; but there are some important differences in the spatial distribution of the eddy kinetic energy within the storm track. The eastern maximum to the northwest of Tharsis still exists, but has decreased in magnitude, and now the primary maximum of eddy kinetic energy is centered around 60°N 120°E. In addition, the overall storm track is less distinct, with weaker gradients at the edges.

The longer averaging period has little effect on the spatial distribution of the baroclinic energy conversion: neither the general pattern, nor the magnitude, and the locations of maxima change. The average pattern of the barotropic energy conversion term does not change much either: the minimum around 60°N 100°E has become less distinct and shifted west (now around 80°E), and the magnitudes of the maxima have decreased slightly, but the general pattern is the same. The energy transport term, as one would expect with smaller horizontal gradients in eddy kinetic energy, is much smaller, and contributes almost nothing to the full seasonal mean, as opposed to the 50-Sol winter solstice period where it was a significant term in some regions. The ageostrophic geopotential flux term changes the most drastically from the 50-Sol mean to the winter mean. The maxima near the high terrain have remained the same, as has the persistent minimum north and east of Tharsis. However, a new, large maximum appears in the area between 50°E, 200°E, 55°N and 75°N.

The fact that the storm track becomes less distinct with a longer averaging time suggests that the storm track changes over the course of the season. Figure 22 shows that this is indeed the case: The western storm track, centered near 70°N 120°E, is the dominant one (and indeed, the only one apparent) for the first third of the winter season, L_s=180°–240°. The middle third of the season is very similar to the top panel of Figure 20 (as would be expected, since those time periods mostly overlap): from L_s=240°–300°, there is a major maximum centered near 60°N 200°E, with a secondary maximum centered near 60°N 130°E. The final third of the winter season features the highest eddy

kinetic energy values, with a primary maximum in the west centered at 65°N 120°E, with a hint of a secondary maximum near 65°N 170°E.

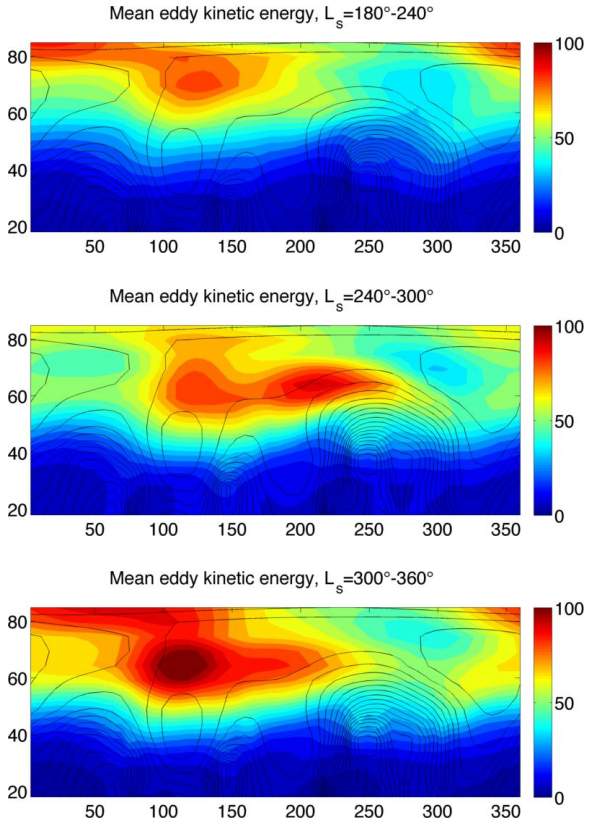

Figure 22: Mean vertically averaged eddy kinetic energy for the beginning (top), middle (middle), and end (bottom) of the winter period.

As mentioned previously, our storm tracks correspond fairly well with those found in modeling studies (e. g. Hollingsworth et al., 1996). However, our results differ significantly from storm tracks found in observational studies (e. g. Banfield et al., 2004; Wang et al., 2005), most significantly in that the most significant observed storm track during the mid- to late-winter appears to be in Acidalia Planitia, between approximately

300°E and 20°E, while models show a relative minimum in storm activity in this area. I believe this is due to differing definitions of storm tracks; most modeling studies use the calculated eddy kinetic energy from the model (as in this study), while observational studies use standard deviations of transient temperature perturbations. In our model, the temperature-derived storm tracks do agree much better with observations, with much more significant activity in the Acidalia region (not shown). The reasons for the large difference in storm track depending on the definition of storm track are unknown, and are beyond the scope of this thesis.

4.2 Regression analysis

Figure 23 shows the result of the regression analysis based on the time series of perturbations of the v component of the wind at the 1 Pa jet level at 65°N, 147°E. Figure 24 is the same, only using the surface pressure at the same point as the basis for the regression. This regression was performed for the first winter period, comprising N=1337 6-hour steps. As with the previous example wave, all variables show signs of vertical tilt, strongly implying baroclinicity of the transient waves. Interestingly, it appears that the tilt is of a different intensity for some variables: the regression of the geopotential height (φ') shows a much steeper tilt than the omega (ω') term. This may just mean that the tilt of the waves is steeper at higher altitudes, since the strongest φ' signal is above the 100 Pa level, while the strongest ω' signal is below the 100 Pa level. This is suggested by the meridional velocity deviation (v') term, which may possibly have a change in slope around the 100 Pa level. Regardless, all fields show coherent,

tilted waves in regression with the deviation from the mean meridional velocity. However, unlike in Chang (1993), there is no clear signal of downstream development in the various fields, especially the v' field. It may be that the downstream transfer of energy is too subtle to appear in the physical fields in the model, or the signal of downstream development may be obscured by the wrapping of waves around the globe due to Mars' much smaller radius. It is also possible that there is no downstream development of waves, and there is some other explanation for the previously described pattern of ageostrophic flux convergence that I have not considered.

Figure 25 shows the vertical cross section of time-lagged regressions for v', using v' at the 1.0 Pa level (left column) and ps' (right column) at (65°N, 147°E) as the basis. The time series of time lags between t=-2 and t=2 day (from top to bottom), shows an eastward propagation of the influences: the past locations where the perturbations have the largest influence on the perturbations at the current time are located upstream, while

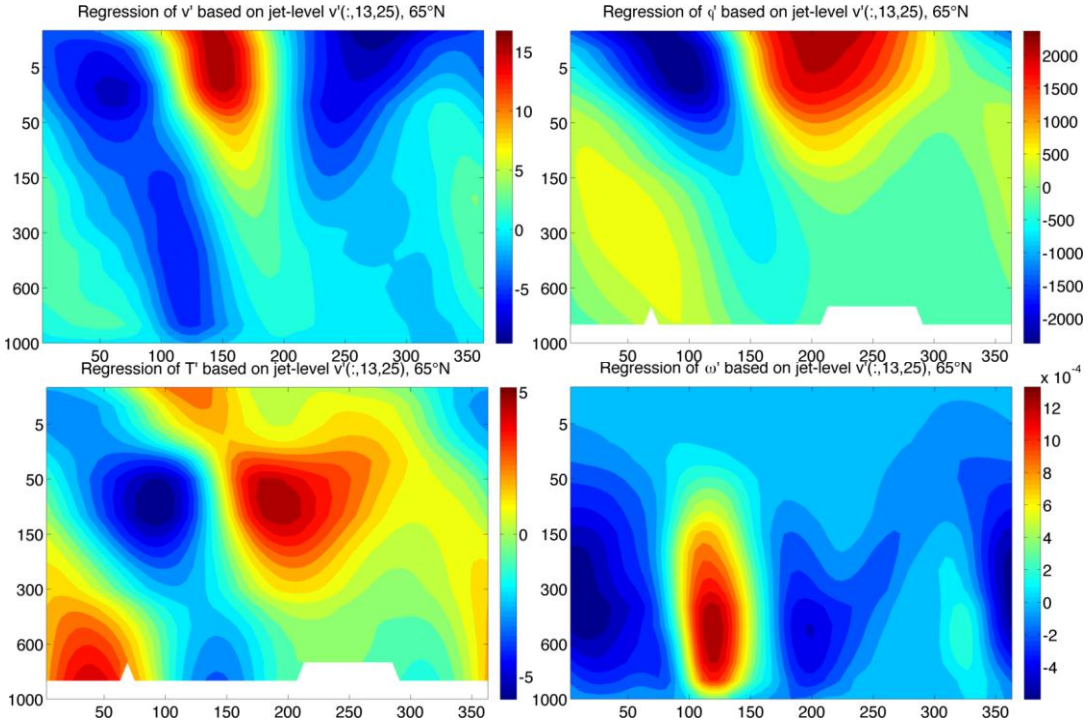

Figure 23: Longitude-height plots at 65°N of regression for *v*', *φ*', *T*', *ω*'. These plots are based on the Winter 1 time series of *v*' 65°N, 147°E at the jet-level (1 Pa)

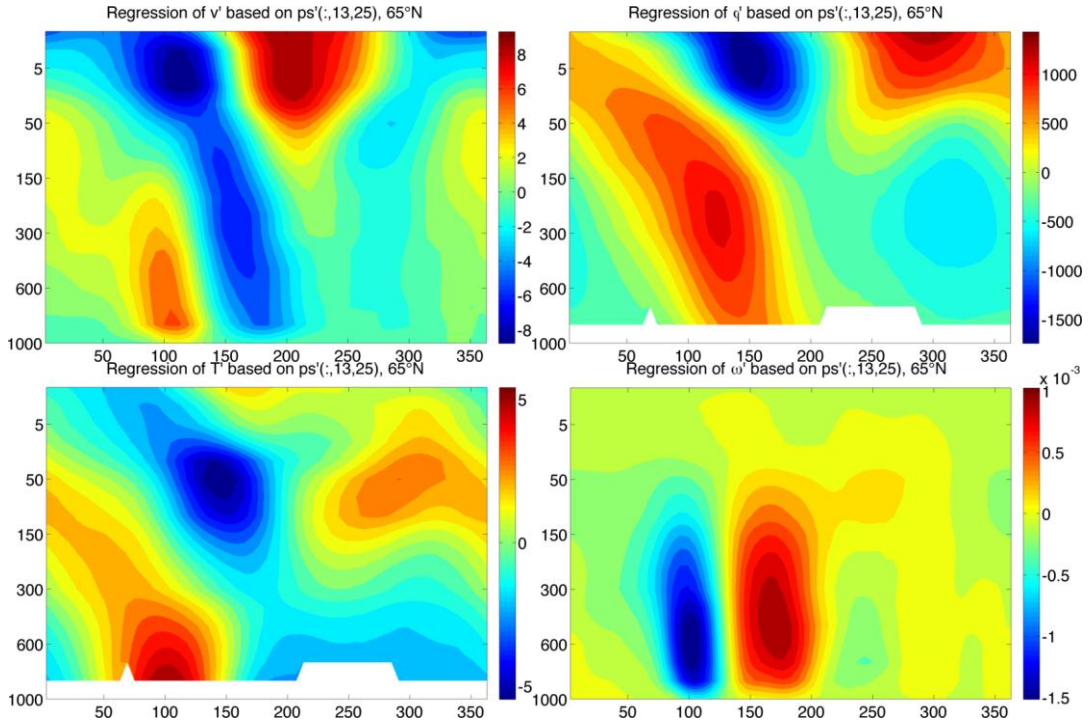

Figure 24: Same as Figure 23, but with surface pressure at 65°N, 147°E used as the regression basis

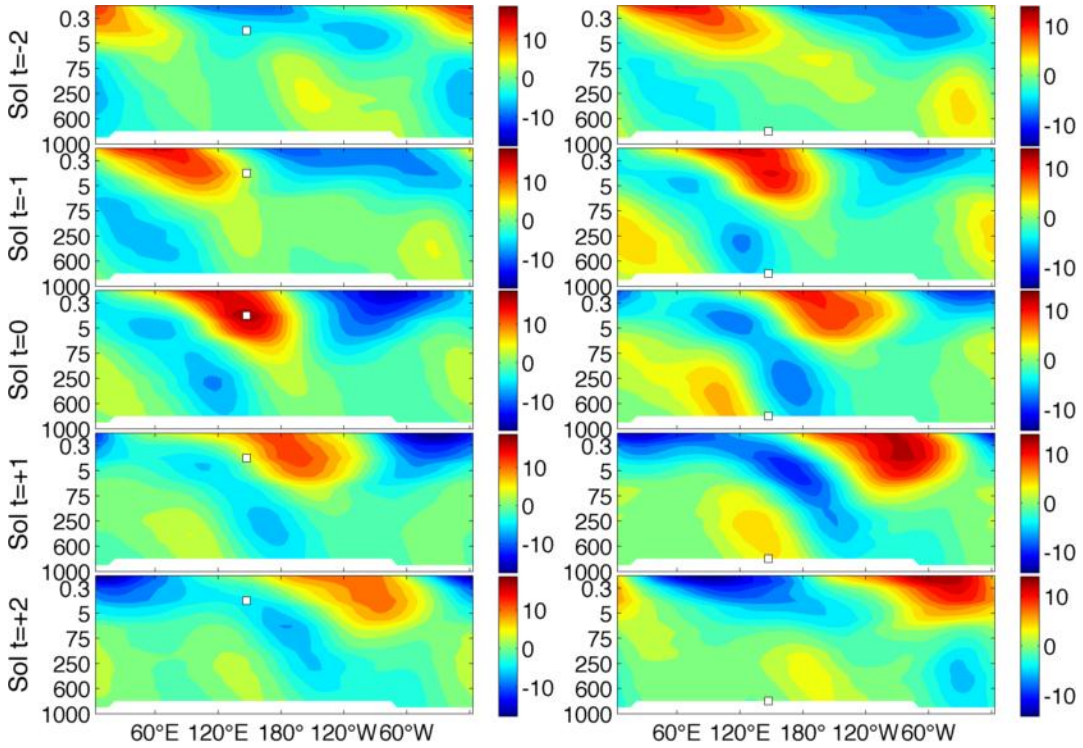

Figure 25: Time-lagged regression for v' based on the jet-level v' (left column) and the surface pressure (right column), both at 65°N, 147°E. Cross section is for 60°N.

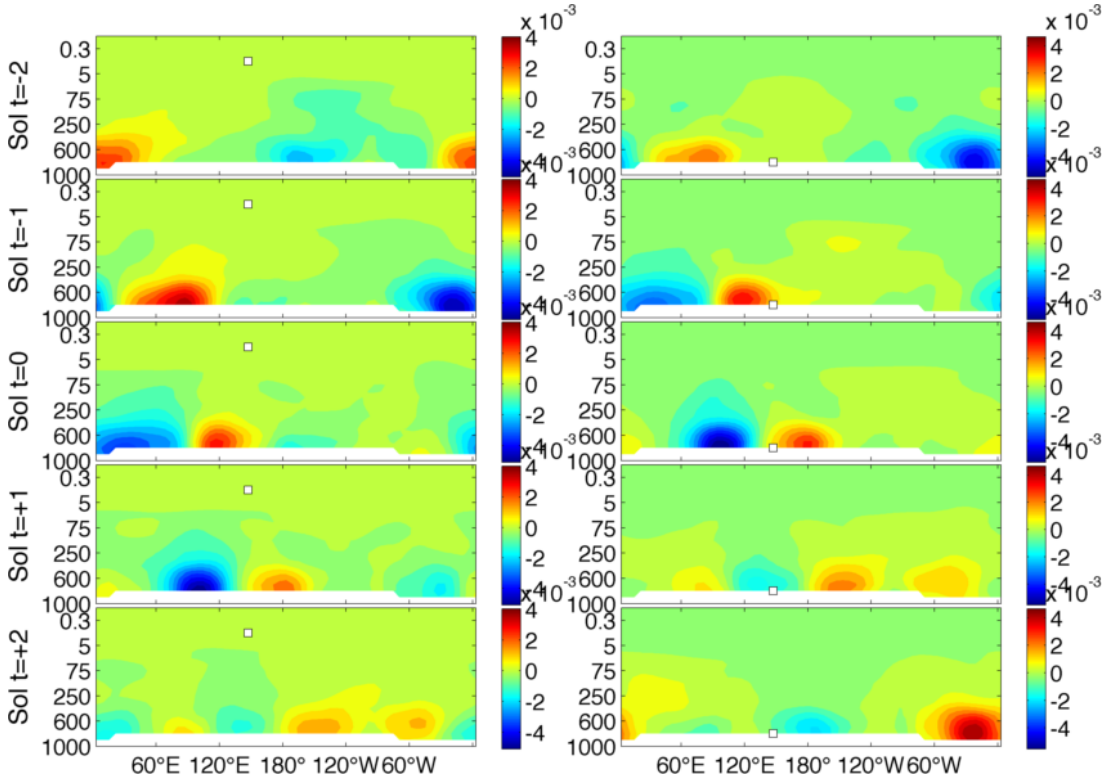

Figure 26:Time-lagged regression for ω'T' based on the jet-level v' (left column) and the surface pressure (right column), both at 65°N, 147°E. Cross section is for 60°N.

the future locations where the perturbations at the current time have the largest influence are located downstream. The regression analysis also indicates influences throughout the entire depth of the atmosphere, which are becoming stronger between Sol -2 and Sol 1 and weakening at Sol 2.

Next I define *y* with the vertical temperature flux $\omega'T'$ instead of the meridional wind perturbation, v' (Figure 26). At time t=-2 Sol, the picture is somewhat noisy, but the vertical temperature flux (baroclinic energy conversion) that has the largest influence on the perturbations at current time are clearly located upstream in the past (centered on 0°E). This influence propagates eastward indicating that the jet level processes are influenced by baroclinic energy conversion upstream and they influence later the baroclinic energy at later times downstream.

4.3 Case study: Winter solstice wave

I choose a wave with especially large values of eddy kinetic energy for a detailed case study. The wave traversed the planet between L_s=261 and L_s=263° (between Sol 686.5 and 690.5 in my numbering system of the days). Figure 27 shows the propagation of the eddy kinetic energy and the surface pressure perturbation. My features of interest are the two spots of eddy kinetic energy maxima centered on 70°N, 0°E and 60°N, 80°E (top left panel). The associated surface feature is a trough (top right panel). The intensity of the two maxima increases for the first four time steps shown, after that it weakens. The eastward propagation of the surface trough is somewhat slower than the propagation

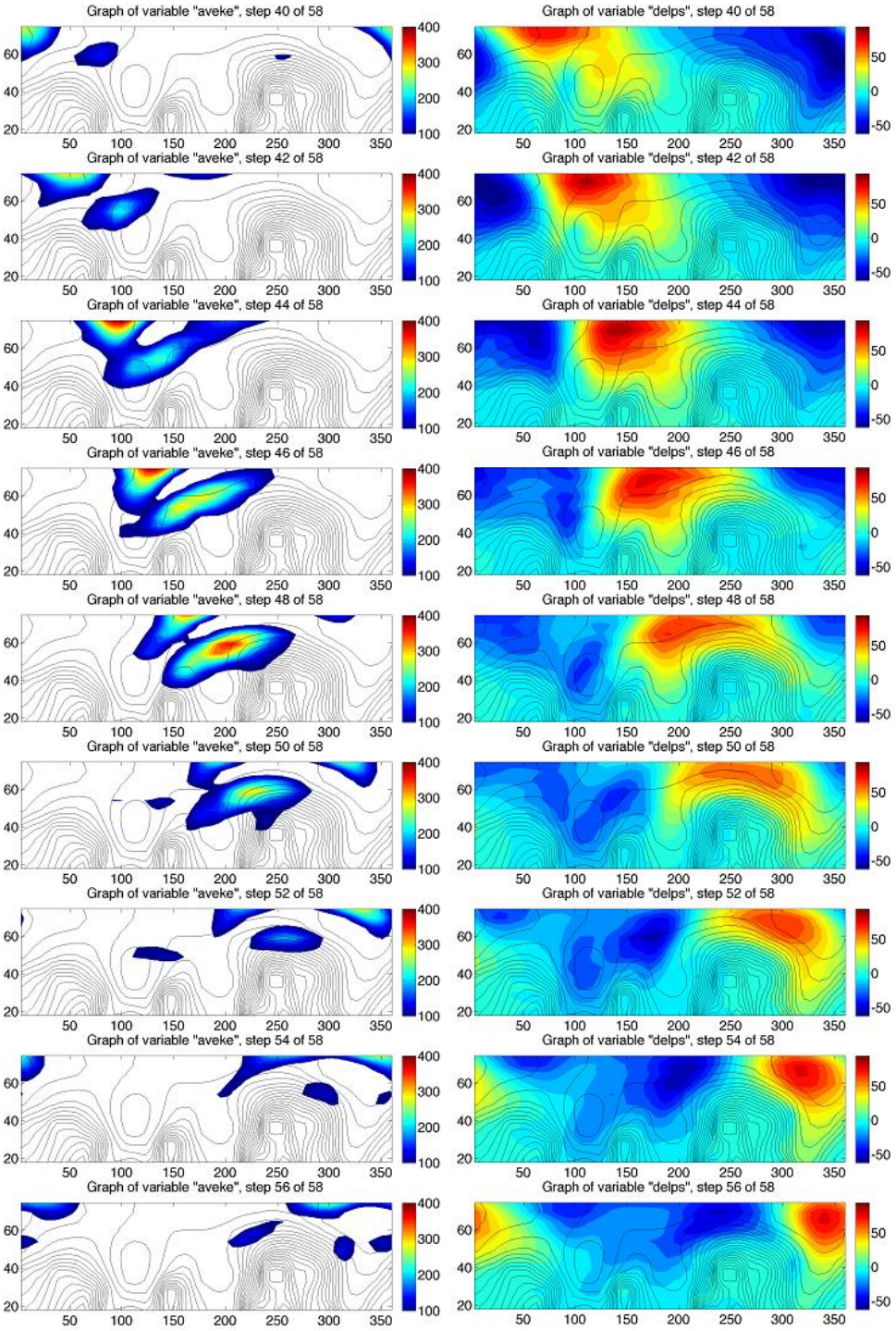

Figure 27: Vertically averaged eddy kinetic energy (left column) and deviation from mean surface pressure (right column) for Winter Solstice wave. The eddy kinetic energy is in units of m^2/s^2, while the surface pressure is in Pa.

of the eddy kinetic energy maxima, and two distinct maxima in the negative surface pressure perturbation appear only at the fourth time step.

Figure 28 shows the baroclinic energy conversion term and the convergence of ageostrophic geopotential fluxes. In this figure, there are two local maxima in the baroclinic energy conversion term at the location of the eddy kinetic energy maxima; although initially the downstream maximum is weak. The intensity of both maxima increases for the next four time steps, suggesting that the increase in the eddy kinetic energy is, at least in part, due to baroclinic energy conversion. Comparing the left and right panels of Figure 28, it is apparent that baroclinic energy conversion is preceded at all locations by a positive contribution of the ageostrophic geopotential fluxes to the eddy kinetic energy: Thus Figure 28 is an indication of the possibility of downstream baroclinic development. (Figure 29, which shows the eddy kinetic energy transport term and barotropic energy conversion does not change the general picture: as can be expected, the eddy kinetic energy is transported downstream, while barotropic energy conversion makes positive and negative contributions near high terrain.)

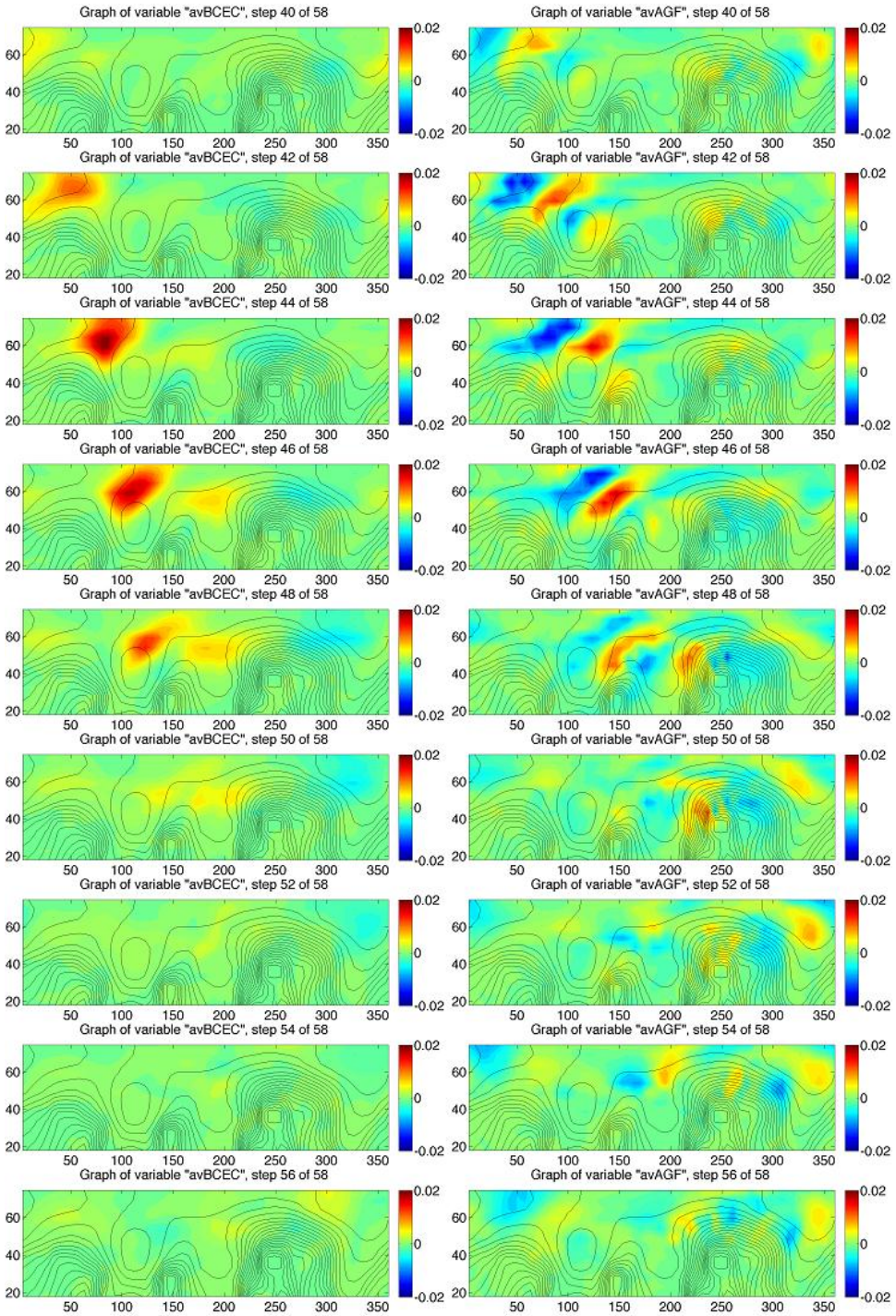

Figure 28: Vertically averaged Baroclinic Energy Conversion (left column) and Ageostrophic Geopotential Flux Convergence (right column). All plots are in units of m^2/s^3.

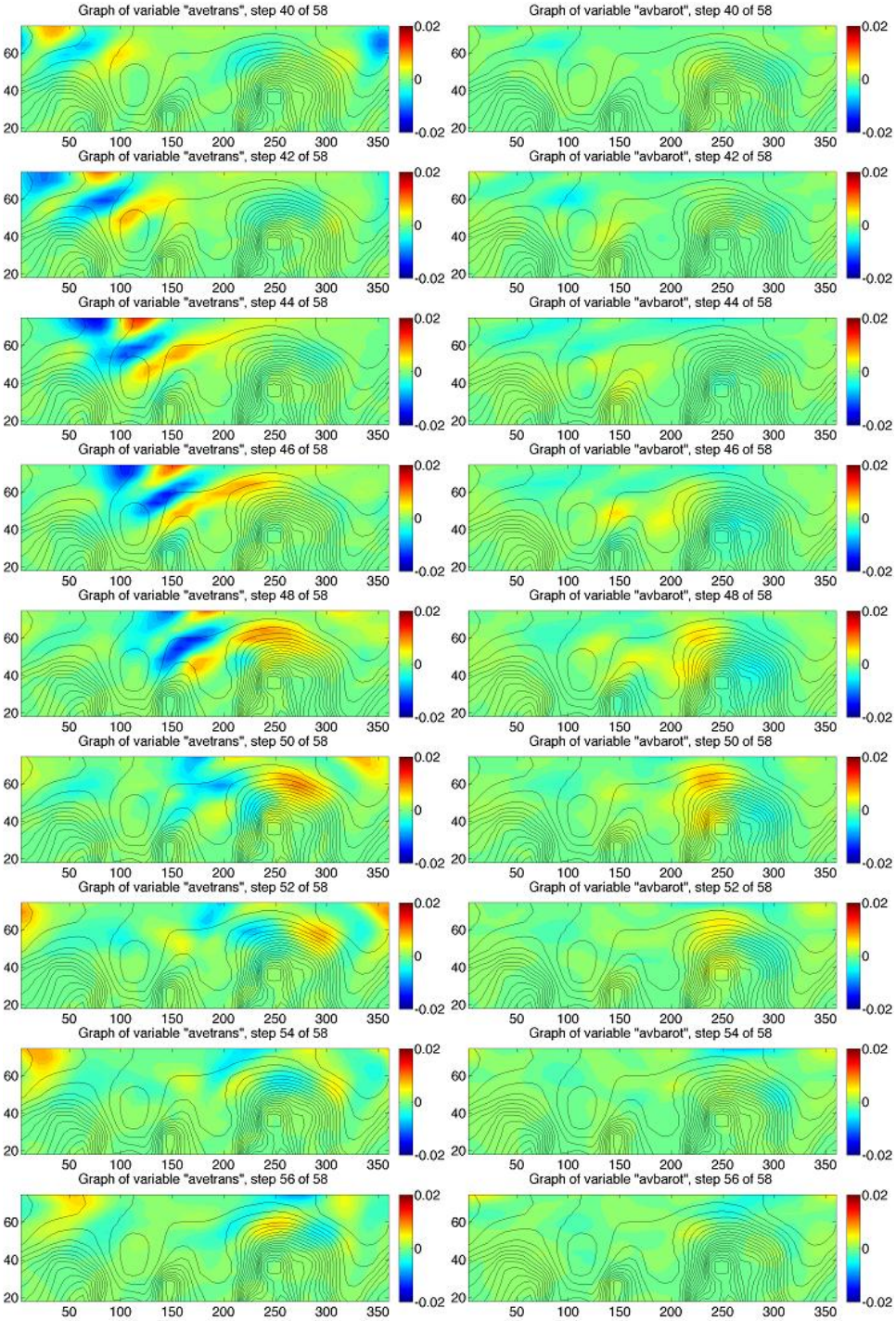

Figure 29: Vertically averaged eddy energy transport (left column) and barotropic energy conversion (right column) for Winter Solstice wave. All plots are in units of m^2/s^3.

5. CONCLUSIONS

Based upon an analysis of the different terms in the eddy kinetic energy derived by Orlanski and Katzfey (1991), as well as a regression analysis based on that performed in Lim and Wallace (1991) and Chang (1993), I suggest that downstream transfer of energy is occurring between different waves in the GFDL Mars General Circulation Model. The temporal average of the baroclinic term confirms that these waves are indeed deriving the main source of their energy from baroclinic instability, with minor contributions from barotropic instabilities, but ageostrophic geopotential fluxes between waves appear to be just as important as they have been found to be on Earth. Regression analyses of the modeled waves suggest that waves which grow via baroclinic energy conversion near the surface grow upward and eventually influence growth at the jet level. In addition, perturbations at the jet level appear to influence later baroclinic growth near the surface. A detailed analysis of an individual wave reveals ageostrophic energy flux from one wave packet initiating baroclinic energy conversion in another. This body of evidence strongly suggests that downstream development of waves occurs in this simulated Martian atmosphere, a result which future studies incorporating real observations should be able to easily confirm or refute.

REFERENCES

Banfield, D., B. J. Conratha, P. J. Gierascha, R. J. Wilson, and M. D. Smith, 2004: Traveling waves in the martian atmosphere from MGS TES Nadir data. *Icarus*, **170,** 365–403, doi:10.1016/j.icarus.2004.03.015.

Barnes, J. R., 1980: Time spectral analysis of midlatitude disturbances in the Martian atmosphere. *J. Atmos. Sci.*, **30,** 2002–2015.

Barnes, J. R., 1981: Midlatitude disturbances in the Martian atmosphere: A second Mars year. *J. Atmos. Sci.*, **38,** 225–234.

Barnes, J. R., J. B. Pollack, R. M. Haberle, C. B. Leovy, R. W. Zurek, H. Lee, and J. Schaeffer, 1993: Mars atmospheric dynamics simulated by the NASA Ames General Circulation Model 2. Transient baroclinic eddies. *J. Geophys. Res.*, **98**, 3125–3148.

Chang, E. K. M., 1993: Downstream development of baroclinic waves as inferred from regression analysis. *J. Atmos. Sci.*, **50,** 2038–2053.

Chang, E. K. M., and Orlanski, I., 1993: On the dynamics of a storm track. *J. Atmos. Sci.*, **50,** 999–1015.

Charney, J. G., 1947: The dynamics of long waves in a baroclinic westerly current. *J. Meteor.*, **4,** 136–162.

Eady, E. T., 1949: Long waves and cyclone waves. *Tellus*, **1,** 33–52, doi:10.1111/j.2153-3490.1949.tb01265.x.

Gierasch, P., P. Thomas, R. French, and J. Veverka. 1979: Spiral clouds on Mars: A new atmospheric phenomenon. *Geophys. Res. Lett.*, **6,** 405–408.

Haberle, R. M., 2002: Planetary atmospheres | Mars. *Encyclopedia of Atmospheric Sciences*, James R. Holton, Judith A Curry and John A. Pyle, Eds., Elsevier Science Ltd., 1745-1755, doi:10.1016/B0-12-227090-8/00312-2.

Hinson, D. P., and R. J. Wilson., 2002: Transient eddies in the southern hemisphere of Mars. *Geophys. Res. Lett.*, **29,** doi:0.1029/2001GL014103.

Hinson, D. P. and H. Wang., 2010: Further observations of regional dust storms and baroclinic eddies in the northern hemisphere of Mars. *Icarus*, **206,** 290–305, doi:10.1016/j.icarus.2009.08.019.

Hollingsworth, J. L., R. M. Haberle, J. R. Barnes, A. F. C. Bridger, J. B. Pollack, H. Lee, and J. Schaeffer, 1996: Orographic control of storm zones on Mars. *Nature*, **380,** 413–416, doi:10.1038/380413a0.

Holton, J. R., 2004: *An Introduction to Dynamic Meteorology*. 4th ed., Elsevier Academic Press, 535 pp.

Hoskins, B. J., and P. J. Valdes, 1990: On the existence of storm tracks. *J. Atmos. Sci.*, **47,** 1854–1864.

James, I. N., 1994: *Introduction to Circulating Atmospheres*. Press Syndicate of the University of Cambridge, 442 pp.

James, P. B., H. H. Kieffer, and D. A. Paige, 1992: The seasonal cycle of carbon dioxide on Mars. *Mars*, H. H. Kieffer, B. M. Jakosky, C. W. Snyder, and M. S. Matthews, Eds., The University of Arizona Press, 934–968.

Kleinböhl, A., J. T. Schofield, D. M. Kass, W. A. Abdou, C. R. Backus and Coauthors, 2009: Mars Climate Sounder limb profile retrieval of atmospheric temperature,

pressure, and dust and water ice opacity. *J.Geophys. Res.*, **114,** 413–416, doi:10.1029/2009JE003358.

Leovy, C. B., G. A. Briggs, A. T. Young, B. A. Smith, J. B. Pollack, E. N. Shipley, and R. L. Wildey, 1972: The Martian atmosphere: Mariner 9 television experiment progress report. *Icarus*, **17,** 373–393, doi:10.1016/0019-1035(72)90006-1.

Leovy, C., 2001: Weather and climate on Mars. *Nature*, **412,** 245–249, doi:10.1038/35084192.

Lim, G. H., and J. M. Wallace, 1991: Structure and evolution of baroclinic waves as inferred from regression analysis. *J. Atmos. Sci.*, **48,** 1718–1732.

Lorenz, Ralph D., 2008: Atmospheric electricity hazards. *Space Sci. Rev.*, **137,** 287–294, doi:10.1007/s11214-008-9364-x.

MOLA Science Team, Mars Global Surveyor, NASA, 2007: The Mars Orbiter Laser Altimeter: Image gallery. [Available online at http://mola.gsfc.nasa.gov/images.html.]

Murphy, J. R. and S. Nelli, 2002: Mars Pathfinder convective vortices: Frequency of occurrence. *Geophys. Res. Lett.*, **29,** doi:10.1029/2002GL015214.

Orlanski, I., and J. Katzfey, 1991: The life cycle of a cyclone wave in the southern hemisphere. Part I: ddy energy budget. *J. Atmos. Sci.*, **48,** 1972–1998.

Orlanski, I., and J. P. Sheldon, 1995: Stages in the energetics of baroclinic systems. *Tellus*, **47,** 605–628, doi:10.1034/j.1600-0870.1995.00108.x.

Oczkowski, M., 2003: Scenarios for the development of locally low dimensional atmospheric dynamics. Dissertation, University of Maryland, 66 pp.

Read, P. L., and S. R. Lewis, 2004: *The Martian Climate Revisited: Atmosphere and Environment of a Desert Planet.* Praxis Publishing Ltd, 326 pp.

Seibert, M., J. Herman, and D. ElDeeb, 2009: Operations strategies for the Mars Exploration Rovers during the 2007 Martian global dust storm. *Proc. 2009 IEEE Aerospace conference*, Big Sky, MT, IEEE, doi:10.1109/AERO.2009.4839697.

Sharma, R., C. A. Wyatt, Jing Zhang, C. I. Calle, N. Mardesich and M. K. Mazumder, 2009: Experimental evaluation and analysis of electrodynamic screen as dust mitigation technology for future Mars missions. *IEEE Trans. Ind. Appl.*, **45,** 591–596, doi:10.1109/TIA.2009.2013542.

Sheehan, W. 1996: *The Planet Mars: A History of Observation and Discovery.* The University of Arizona Press, 270 pp.

Smith, M. D., M. J. Wolff, M. T. Lemmon, N. Spanovich, D. Banfield, and Coauthors, 2004: First atmospheric science results from the Mars Exploration Rovers Mini-TES. *Science*, **306,** 1750–1753, doi:10.1126/science.1104257.

Smith, M. D., 2009: THEMIS observations of Mars aerosol optical depth from 2002–2008. *Icarus*, **202,** 444–452, doi:10.1016/j.icarus.2009.03.027.

Wang, H., R. W. Zurek, and M. I. Richardson, 2005: Relationship between frontal dust storms and transient eddy activity in the northern hemisphere of Mars as observed by Mars Global Surveyor. *J.Geophys. Res.*, **110,** 20, doi:10.1029/2005JE002423.

Zimin, A. V., I. Szunyogh, D. J. Patil, B. R. Hunt, and E. Ott., 2003: Extracting envelopes of Rossby wave packets. *Mon. Weather Rev.*, **131,** 1011–1017.

VITA

Name:	Michael J. Kavulich Jr.
Address:	Department of Atmospheric Sciences, MS 3150, Texas A&M University, College Station, Texas 77843-3150.
Email Address:	michael.j.kavulich.jr@gmail.com
Education:	B.S., Physics, Worcester Polytechnic Institute, 2008 M.S., Atmospheric Sciences, Texas A&M University, 2011